Published by Institute of Physics Publishing for SISSA
Received: *January 7, 2005*
Revised: *April 30, 2005*
Accepted: *May 12, 2005*
Published: *June 10, 2005*

Measurement of the gluino mass via cascade decays for SPS 1a

Børge Kile Gjelsten
Department of Physics, University of Oslo
N-0316 Oslo, Norway
E-mail: B.K.Gjelsten@fys.uio.no

David John Miller
Department of Physics and Astronomy, University of Glasgow
Glasgow G12 8QQ, U.K.
E-mail: D.Miller@physics.gla.ac.uk

Per Osland
Department of Physics and Technology, University of Bergen
N-5007 Bergen, Norway, and
TH Division, Physics Department, CERN
CH 1211 Genève, Switzerland
E-mail: Per.Osland@ift.uib.no

Abstract: If R-parity conserving supersymmetry is realised with masses below the TeV scale, sparticles will be produced and decay in cascades at the LHC. In the case of a neutral LSP, which will not be detected, decay chains cannot be fully reconstructed, complicating the mass determination of the new particles. In this paper we extend the method of obtaining masses from kinematical endpoints to include a gluino at the head of a five-sparticle decay chain. This represents a non-trivial extension of the corresponding method for the squark decay chain. We calculate the endpoints of the new distributions and assess their applicability by examining the theoretical distributions for a variety of mass scenarios. The precision with which the gluino mass can be determined by this method is investigated for the mSUGRA point SPS 1a. Finally we estimate the improvement obtained from adding a Linear Collider measurement of the LSP mass.

Keywords: Supersymmetry Phenomenology, Supergravity Models.

JHEP06(2005)015

Contents

1. Introduction

Supersymmetry [1 − 4] provides one of the more popular extensions to the Standard Model at higher energies. It has many attractive features, one of which is a possible solution to the hierarchy problem [5]. For this to be the case supersymmetric particles must exist near the TeV-scale, and may therefore be accessed by the LHC.

Conservation of R-parity means that any interaction vertex must involve an even number of supersymmetric fields. For collider experiments this has two important consequences: sparticles will be produced in pairs, and the decay chain of a sparticle will always end with the lightest supersymmetric particle (LSP). A SUSY event at the LHC will then result in two decay chains, each giving an undetected LSP together with a number of detectable Standard Model particles. The escaping LSPs make it difficult to fully reconstruct events. This means that the masses of the sparticles involved in a decay chain cannot be readily reconstructed from the end products. However, even though they do not represent any particular sparticle, the various mass distributions that can be constructed from the detectable particles of the decay do have a sensitivity to the sparticle masses. In particular, the maximum value of each of these distributions can in principle be calculated for any given decay chain, and this maximum value will be determined by the masses involved in the decay. If these kinematical endpoints are measured, it is then possible to obtain the sparticle masses in a numerical fit. This 'endpoint method' has been widely used to determine masses of supersymmetric particles [6 − 11]. The decay chain

$$\tilde{q}_L \to \tilde{\chi}_2^0 q_{\mathrm{f}} \to \tilde{l}_R l_{\mathrm{n}} q_{\mathrm{f}} \to \tilde{\chi}_1^0 l_{\mathrm{f}} l_{\mathrm{n}} q_{\mathrm{f}} \tag{1.1}$$

is particularly amenable to this method[1]. In [12] we investigated this decay chain in considerable detail for two points on the SPS 1a line [13]: (α), which is the standard point and often simply referred to as 'the SPS 1a point', and (β), which lies at somewhat higher masses. In this paper we restrict ourselves to the standard SPS 1a point and investigate the situation where a gluino is at the head of the decay chain,

$$\tilde{g} \to \tilde{q}_L q_{\mathrm{n}} \to \tilde{\chi}_2^0 q_{\mathrm{f}} q_{\mathrm{n}} \to \tilde{l}_R l_{\mathrm{n}} q_{\mathrm{f}} q_{\mathrm{n}} \to \tilde{\chi}_1^0 l_{\mathrm{f}} l_{\mathrm{n}} q_{\mathrm{f}} q_{\mathrm{n}}\,. \tag{1.2}$$

Seven more distributions become available with the inclusion of q_{n}, and their endpoints, if measurable, will enable us to find the gluino mass. For ease of reference the new distributions/endpoints will be called 'gluino distributions/endpoints' as opposed to the 'squark distributions/endpoints' which do not involve the gluino mass.

Although very much in line with the now standard method for the masses involved in (1.1), this way of obtaining the gluino mass is new. At present two other methods are proposed. One is an approximate technique, used for example in [14]. If, in the three-body decay $\tilde{\chi}_2^0 \to \tilde{\chi}_1^0 ll$, we have m_{ll} at its maximum value, $m_{ll} = m_{ll}^{\max}$, then $\tilde{\chi}_1^0$ is at rest

[1] Maintaining the standard convention, the subscripts 'n' for *near* and 'f' for *far* on the leptons and quarks are used to distinguish the order of particle emission in the decay chain. These subscripts will be suppressed if there is no ambiguity. In [12], which will be frequently referred to throughout the text, no subscript is used for the quark as there is only one. In the current notation this quark corresponds to q_{f}.

JHEP06(2005)015

in the rest frame of $\tilde{\chi}_2^0$. Assuming $m_{\tilde{\chi}_1^0}$ known, the four-vector of $\tilde{\chi}_2^0$ can then be fully reconstructed. Next, adding the two quark four-momenta provides us with the complete four-momentum of the gluino (and squark). This allows the mass of the gluino (and the squark) to be found in the more traditional way of plotting the mass peak. Apart from the normal experimental uncertainties this method is exact. However, for the decay chain (1.2), it is generally not the case that $\tilde{\chi}_1^0$ is at rest in the rest frame of $\tilde{\chi}_2^0$ when $m_{ll} = m_{ll}^{\max}$. Only if $m_{\tilde{l}_R}^2 = m_{\tilde{\chi}_2^0} m_{\tilde{\chi}_1^0}$ is this true, and the more this relation is violated, the less reliable the results will become. Furthermore, to get a sizable sample, also events with m_{ll} somewhat below $m_{ll}^{\max}$ must be used, which increases the uncertainty of the resulting masses. So, to apply this method to (1.2) the following three effects must be controlled: i) the knowledge of $m_{\tilde{\chi}_1^0}$ — this can be assumed known from the standard endpoint analysis of the squark chain, but the appropriate uncertainties must be included, ii) the systematics from the violation of $m_{\tilde{l}_R}^2 = m_{\tilde{\chi}_2^0} m_{\tilde{\chi}_1^0}$, and iii) the systematics from the inclusion of events with $m_{ll} < m_{ll}^{\max}$. A rigorous treatment of all these effects is still wanting.

The other method to obtain the gluino mass from (1.2) goes under the name of the 'Mass relation method', and is described in [15]. In a first version the masses of $\tilde{\chi}_1^0$, $\tilde{l}_R$ and $\tilde{\chi}_2^0$ are assumed known, e.g. from the squark-endpoint analysis. For a given gluino-chain event we then have six unknowns: $m_{\tilde{g}}$, $m_{\tilde{q}_L}$ and the four-momentum of $\tilde{\chi}_1^0$. On-shell mass conditions for the five sparticles provide five equations. For *one* such event we are one condition short of determining the system. (If also $m_{\tilde{q}_L}$ is assumed known, the system is solvable.) A second event of the same type will again give 5 equations for 6 unknowns. Two of the unknowns, $m_{\tilde{g}}$ and $m_{\tilde{q}_L}$ are however the same for the two events. In combination one therefore has 10 equations for 10 unknowns. The system can be solved analytically to provide (in some cases multiple) masses for the gluino and the squark. The mass relation method involves no approximations of the type described for the first method, and is in this respect at the same level as the endpoint method we will use here. The mass relation method also has the advantage that it avoids the difficulties related to estimating endpoints, and it can give a measurement even for quite a small number of events. On the other hand the uncertainties on the three lighter masses as well as possible correlations between the masses need to be appropriately handled. An extension of the method to take no input masses, and/or include in a consistent way measurements from an endpoint analysis should be feasible and would meet these requirements.

For the endpoint method, which in the following is developed to also provide the gluino mass, all measurements go into the same fit, so errors and correlations are automatically treated correctly.

The structure of the present paper is as follows. In section 2 we present the endpoints of the invariant distributions associated with gluino decays. We also discuss the ambiguity which arises from having two quarks in the final state and plot some examples of gluino distributions with no experimental effects. Section 3 presents a simulation of the gluino endpoints at the ATLAS detector for the benchmark SUSY scenario SPS 1a, ending with an estimate for some of the new endpoints. Energy scale errors are also discussed in some detail. In section 4 values for masses and mass differences are found from the estimates of the endpoint measurements. In section 5 the impact of the statistical error is separated from that of the energy scale error and two somewhat more conservative error scenarios are studied. The effect of adding a Linear Collider measurement is investigated in section 6, while conclusions are made in section 7. A new method for calculating $m_{q_{\rm f}ll}^{\max}$ is developed and generalised to the gluino case $m_{qqll}^{\max}$ in appendix A. Finally, the complicated gluino endpoint $m_{qql(\rm low)}^{\max}$ is derived in some detail in appendix B.

2. Gluino endpoints

2.1 Endpoint calculation

Using the method detailed in appendix A we obtain the maximum value of m_{qqll} for the five-sparticle gluino chain:

$$\left(m_{qqll}^{\max}\right)^2 = \begin{cases} \frac{\left(m_{\tilde g}^2-m_{\tilde q_L}^2\right)\left(m_{\tilde q_L}^2-m_{\tilde\chi_1^0}^2\right)}{m_{\tilde q_L}^2} & \text{for} \quad \frac{m_{\tilde g}}{m_{\tilde q_L}} > \frac{m_{\tilde q_L}}{m_{\tilde\chi_2^0}}\frac{m_{\tilde\chi_2^0}}{m_{\tilde l_R}}\frac{m_{\tilde l_R}}{m_{\tilde\chi_1^0}} \quad (1) \\ \frac{\left(m_{\tilde g}^2 m_{\tilde\chi_2^0}^2-m_{\tilde q_L}^2 m_{\tilde\chi_1^0}^2\right)\left(m_{\tilde q_L}^2-m_{\tilde\chi_2^0}^2\right)}{m_{\tilde q_L}^2 m_{\tilde\chi_2^0}^2} & \text{for} \quad \frac{m_{\tilde q_L}}{m_{\tilde\chi_2^0}} > \frac{m_{\tilde\chi_2^0}}{m_{\tilde l_R}}\frac{m_{\tilde l_R}}{m_{\tilde\chi_1^0}}\frac{m_{\tilde g}}{m_{\tilde q_L}} \quad (2) \\ \frac{\left(m_{\tilde g}^2 m_{\tilde l_R}^2-m_{\tilde\chi_2^0}^2 m_{\tilde\chi_1^0}^2\right)\left(m_{\tilde\chi_2^0}^2-m_{\tilde l_R}^2\right)}{m_{\tilde\chi_2^0}^2 m_{\tilde l_R}^2} & \text{for} \quad \frac{m_{\tilde\chi_2^0}}{m_{\tilde l_R}} > \frac{m_{\tilde l_R}}{m_{\tilde\chi_1^0}}\frac{m_{\tilde g}}{m_{\tilde q_L}}\frac{m_{\tilde q_L}}{m_{\tilde\chi_2^0}} \quad (3) \\ \frac{\left(m_{\tilde g}^2-m_{\tilde l_R}^2\right)\left(m_{\tilde l_R}^2-m_{\tilde\chi_1^0}^2\right)}{m_{\tilde l_R}^2} & \text{for} \quad \frac{m_{\tilde l_R}}{m_{\tilde\chi_1^0}} > \frac{m_{\tilde g}}{m_{\tilde q_L}}\frac{m_{\tilde q_L}}{m_{\tilde\chi_2^0}}\frac{m_{\tilde\chi_2^0}}{m_{\tilde l_R}} \quad (4) \\ \left(m_{\tilde g}-m_{\tilde\chi_1^0}\right)^2 & \text{otherwise} \quad (5) \end{cases} \tag{2.1}$$

Notice the systematic form of the defining inequalities and the resemblence to $m_{q_{\rm f}ll}^{\max}$, given in [12, eq. (4.4)]. For the gluino endpoint we have four 'dominance regions', each defined in terms of a nearest-neighbour mass ratio dominating the product of the three others. As before, simplifications can be made to these inequalities, but with the undesired consequence of obscuring the neat and systematic structure.

In principle, a measurement of $m_{qqll}^{\max}$ would, in combination with the squark endpoints, suffice to provide the gluino mass. The long decay chain does however allow for more distributions to be constructed, from which endpoints can be extracted and compared with analytic expressions. These other available endpoints are useful both as over-constraining measurements and as consistency tests.

The gluino chain has seven primary endpoints which involve $m_{\tilde g}$. The two-particle primary endpoints $m_{qq}^{\max}$, $m_{q_{\rm n}l_{\rm n}}^{\max}$, $m_{q_{\rm n}l_{\rm f}}^{\max}$ are easily calculated from cascade decays 'on a line'. There is only one realisation for each.

For the three-particle endpoint $m_{qql_{\rm n}}^{\max}$, the particles involved are neighbours in the decay chain, giving a situation similar to $m_{q_{\rm f}ll}^{\max}$. The solution can be found from [12, eq. (4.4)] via the substitutions

$$(m_{\tilde q_L}, m_{\tilde\chi_2^0}, m_{\tilde l_R}, m_{\tilde\chi_1^0}) \rightarrow (m_{\tilde g}, m_{\tilde q_L}, m_{\tilde\chi_2^0}, m_{\tilde l_R}) \tag{2.2}$$

in both the endpoint expressions and the inequalities.

The two other three-particle endpoints $m_{q_\mathrm{n}ll}^{\max}$ and $m_{qql_\mathrm{f}}^{\max}$ are more difficult to find because the particles involved are not all nearest neighbours in the decay chain. However, it is possible to transform the problem into one which involves only nearest neighbours. Let us first consider $m_{q_\mathrm{n}ll}^{\max}$. The initial point of difficulty is the orientation of the $\tilde{q}_L$ decay, where the unused q_f is emitted. Will the orientation which gives the largest $m_{q_\mathrm{n}ll}$ depend on the mass scenario? To answer this question, boost to the rest frame of $\tilde{\chi}_2^0$. Whatever the details of the two steps prior to the creation of $\tilde{\chi}_2^0$, at this stage the only quantity of relevance to $m_{q_\mathrm{n}ll}$ is $|\mathbf{p}_{q_\mathrm{n}}|$. The larger the momentum is, the larger $m_{q_\mathrm{n}ll}$ can become. Thus, independent of masses, for maximum values of $m_{q_\mathrm{n}ll}$, the orientation of the $\tilde{q}_L$ decay is always the one that maximises $|\mathbf{p}_{q_\mathrm{n}}|$ in the rest frame of $\tilde{\chi}_2^0$. This means sending $\tilde{\chi}_2^0$ in the opposite direction of q_n, and the configuration which gives $m_{q_\mathrm{n}ll}^{\max}$ therefore has $\mathbf{p}_{q_\mathrm{n}}$ parallel to $\mathbf{p}_{q_\mathrm{f}}$.

With this point settled, the situation can be transformed into a nearest-neighbour decay, for which we know the solution. To do this we introduce a pseudo-particle: as seen from the rest frame of $\tilde{\chi}_2^0$ the momentum of q_n corresponds to the decay of a pseudo-particle $Y \to \tilde{\chi}_2^0 q_\mathrm{n}$ with mass $m_Y^2 = m_{\tilde{g}}^2 - m_{\tilde{q}_L}^2 + m_{\tilde{\chi}_2^0}^2$. In such a picture all particles are nearest neighbours, and the solution [12, eq. (4.4)] applies with the appropriate substitution

$$m_{\tilde{q}_L} \to m_Y = \sqrt{m_{\tilde{g}}^2 - m_{\tilde{q}_L}^2 + m_{\tilde{\chi}_2^0}^2}\,. \tag{2.3}$$

For $m_{qql_\mathrm{f}}^{\max}$ the orientation of the $\tilde{\chi}_2^0$ decay is fixed to maximise $|\mathbf{p}_{l_\mathrm{f}}|$ in the rest frame of $\tilde{\chi}_2^0$, analogous to the argument above. Another pseudo-particle is then defined at the end of the decay chain, $\tilde{\chi}_2^0 \to Y l_\mathrm{f}$ where $m_Y = m_{\tilde{\chi}_1^0} m_{\tilde{\chi}_2^0}/m_{\tilde{l}_R}$. Again, the problem has been reformulated in terms of nearest neighbours, so solution [12, eq. (4.4)] applies. The appropriate substitutions are

$$(m_{\tilde{q}_L}, m_{\tilde{\chi}_2^0}, m_{\tilde{l}_R}, m_{\tilde{\chi}_1^0}) \to \left(m_{\tilde{g}}, m_{\tilde{q}_L}, m_{\tilde{\chi}_2^0}, \frac{m_{\tilde{\chi}_1^0} m_{\tilde{\chi}_2^0}}{m_{\tilde{l}_R}} \right). \tag{2.4}$$

As was discussed for the squark chain, primary distributions based on distinguishing the two leptons can in practice not be constructed. Instead of the distributions $m_{q_\mathrm{n}l_\mathrm{n}}$, $m_{q_\mathrm{n}l_\mathrm{f}}$, m_{qql_n} and m_{qql_f} one can construct $m_{q_\mathrm{n}l(\mathrm{high})}$, $m_{q_\mathrm{n}l(\mathrm{low})}$, $m_{qql(\mathrm{high})}$ and $m_{qql(\mathrm{low})}$. While the endpoint of a 'high' distribution is simply the maximum of the two primary endpoints for the given mass scenario, further considerations are needed for the 'low' distributions. For $m_{q_\mathrm{n}l(\mathrm{low})}$ these considerations are quite manageable, but for the three-particle distribution $m_{qql(\mathrm{low})}$ they become rather involved. The general solution for the latter is given in appendix B.

The endpoint expressions are summarised below. Together with eq. (2.1), the six first ones, eqs. (2.5)–(2.10), correspond to the distributions which are usable in that they do not rely on distinguishing the two leptons:

$$\left(m_{qq}^{\max}\right)^2 = \left(m_{\tilde{g}}^2 - m_{\tilde{q}_L}^2\right) \frac{\left(m_{\tilde{q}_L}^2 - m_{\tilde{\chi}_2^0}^2\right)}{m_{\tilde{q}_L}^2} \tag{2.5}$$

$$m_{qql(\text{low})}^{\max} \ : \ \text{see appendix B} \tag{2.6}$$

$$m_{qql(\text{high})}^{\max} = \max(m_{qql_\text{n}}^{\max}, m_{qql_\text{f}}^{\max}) \tag{2.7}$$

$$m_{q_\text{n}ll}^{\max} \ : \ [12, \text{eq. } (4.4)] \text{ with } m_{\tilde{q}_L} \rightarrow \sqrt{m_{\tilde{g}}^2 - m_{\tilde{q}_L}^2 + m_{\tilde{\chi}_2^0}^2} \tag{2.8}$$

$$m_{q_\text{n}l(\text{low})}^{\max} = \max(m_{q_\text{n}l_\text{n}}^{\max}, m_{q_\text{n}l(\text{eq})}^{\max}) \tag{2.9}$$

$$m_{q_\text{n}l(\text{high})}^{\max} = \max(m_{q_\text{n}l_\text{n}}^{\max}, m_{q_\text{n}l_\text{f}}^{\max}) \tag{2.10}$$

$$\left(m_{q_\text{n}l_\text{n}}^{\max}\right)^2 = \left(m_{\tilde{g}}^2 - m_{\tilde{q}_L}^2\right) \frac{\left(m_{\tilde{\chi}_2^0}^2 - m_{\tilde{l}_R}^2\right)}{m_{\tilde{\chi}_2^0}^2} \tag{2.11}$$

$$\left(m_{q_\text{n}l_\text{f}}^{\max}\right)^2 = \left(m_{\tilde{g}}^2 - m_{\tilde{q}_L}^2\right) \frac{\left(m_{\tilde{l}_R}^2 - m_{\tilde{\chi}_1^0}^2\right)}{m_{\tilde{l}_R}^2} \tag{2.12}$$

$$\left(m_{q_\text{n}l(\text{eq})}^{\max}\right)^2 = \left(m_{\tilde{g}}^2 - m_{\tilde{q}_L}^2\right) \frac{\left(m_{\tilde{l}_R}^2 - m_{\tilde{\chi}_1^0}^2\right)}{\left(2m_{\tilde{l}_R}^2 - m_{\tilde{\chi}_1^0}^2\right)} \tag{2.13}$$

$$m_{qql_\text{n}}^{\max} \ : \ [12, \text{eq. } (4.4)] \text{ with } (m_{\tilde{q}_L}, m_{\tilde{\chi}_2^0}, m_{\tilde{l}_R}, m_{\tilde{\chi}_1^0}) \rightarrow (m_{\tilde{g}}, m_{\tilde{q}_L}, m_{\tilde{\chi}_2^0}, m_{\tilde{l}_R}) \tag{2.14}$$

$$m_{qql_\text{f}}^{\max} \ : \ [12, \text{eq. } (4.4)] \text{ with } (m_{\tilde{q}_L}, m_{\tilde{\chi}_2^0}, m_{\tilde{l}_R}, m_{\tilde{\chi}_1^0}) \rightarrow \left(m_{\tilde{g}}, m_{\tilde{q}_L}, m_{\tilde{\chi}_2^0}, \frac{m_{\tilde{\chi}_1^0} m_{\tilde{\chi}_2^0}}{m_{\tilde{l}_R}}\right). \tag{2.15}$$

2.2 Quark ambiguity

Adding a gluino to the cascade introduces an additional ambiguity: how does one distinguish between the jet initiated by the gluino decay and that initiated by the squark decay? Initially we will assume that the two correct jets of a signal event have been selected, although we do not know which is which. (The difficulties associated with this assumption will be commented on later.) In this case, one can seek to distinguish the two jets kinematically, by, for example, their transverse momenta. If $m_{\tilde{g}}^2 - m_{\tilde{q}_L}^2$ is very different from $m_{\tilde{q}_L}^2 - m_{\tilde{\chi}_2^0}^2$, the two quarks will be emitted with noticeably different energies, and a p_T comparison will, with a certain purity, serve to distinguish between the jets. However, one cannot, a priori, know which jet is to be assigned to q_n or q_f, i.e. whether it is q_n or q_f which gives rise to the hardest jet, and one must instead turn to the differences in production rates. Only when a gluino sits on top of the chain is q_n produced, and often, the ratio of directly versus indirectly produced squarks is sufficient to determine the average behaviour of q_f. This then allows statements on the average behaviour of q_n and q_f to be made, which

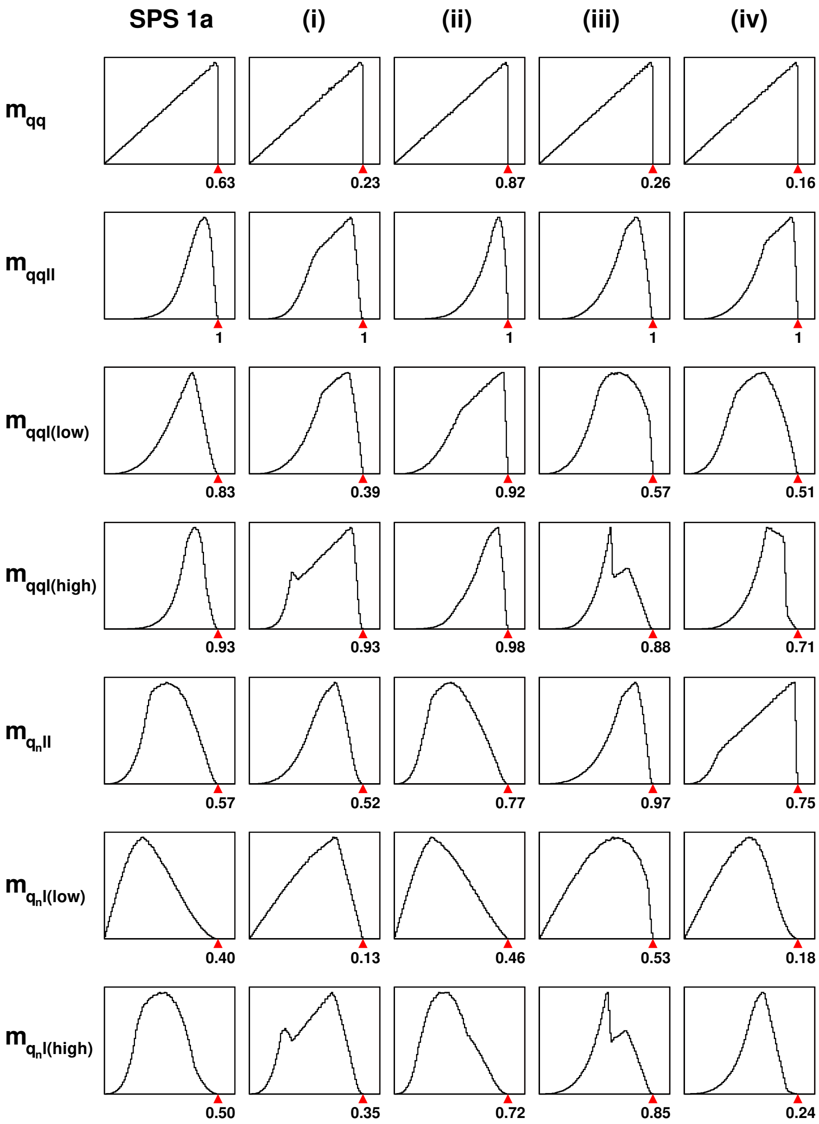

Figure 1: Theory distributions for SPS 1a and four other mass scenarios, showing some of the shape variety. Only gluino distributions are shown. Kinematic endpoints are marked with a triangle and given in units of $m_{qqll}^{\max}$, the largest of the endpoints. (All panels start at zero invariant mass.) The scenarios (i)–(iv) are defined by the following sets of mass ratios $\mathbf{r} \equiv (m_{\tilde{g}}/m_{\tilde{q}_L}, m_{\tilde{q}_L}/m_{\tilde{\chi}_2^0}, m_{\tilde{\chi}_2^0}/m_{\tilde{l}_R}, m_{\tilde{l}_R}/m_{\tilde{\chi}_1^0})$: $\mathbf{r}_{(\mathrm{i})} = (1.03, 1.30, 1.07, 6.01)$, $\mathbf{r}_{(\mathrm{ii})} = (1.79, 3.01, 1.15, 1.59)$, $\mathbf{r}_{(\mathrm{iii})} = (1.45, 1.05, 1.27, 5.08)$ and $\mathbf{r}_{(\mathrm{iv})} = (1.03, 1.29, 2.02, 3.60)$.

may be used to construct samples where the quark identity is required, eqs. (2.8)–(2.10), as well as the squark distributions $m_{q_{\mathrm{f}}ll}$, $m_{q_{\mathrm{f}}l(\mathrm{low})}$ and $m_{q_{\mathrm{f}}l(\mathrm{high})}$. Such a separation of q_{n} and q_{f} will always introduce impurities; whether these are manageable or not will depend on the given SUSY scenario.

To be fully general one might consider constructing new secondary distributions in which there is no need to distinguish the jets. The distributions m_{ll}, m_{qq}, m_{qqll}, $m_{qql(\mathrm{low})}$ and $m_{qql(\mathrm{high})}$ would remain unaffected, but instead of $m_{q_{\mathrm{f}}ll}$ and $m_{q_{\mathrm{n}}ll}$, one should construct new distributions $m_{qll(\text{high})}$ and $m_{qll(\text{low})}$. The endpoint expression of the former is readily available, but not of the latter. The complexity of the calculation and the resulting expression for $m^{\max}_{qll(\text{low})}$ can be expected to be similar to that of $m^{\max}_{qql(\text{low})}$ shown in appendix B. Furthermore, for the four m_{ql} distributions one can collect four new distributions based on the order of the four values per event. Only the endpoint of the $m_{ql(\text{high})}$ distribution is readily available, while the other three endpoints become very difficult to calculate. A programme to calculate the new endpoints where quarks are not distinguished, has so far not been started.

The above discussion shows that as a second jet is added, the complexity of the situation increases significantly. In return many more endpoints become available, allowing for thorough consistency checks. In section 3 we will return to these issues in the context of a simulation at the standard SPS 1a point.

2.3 Theory distributions

In order for the endpoint method to be useful, not only must the analytic expressions for the endpoints be available, it must also be possible to determine these endpoints from the experimental mass distributions. A first criterion for this is that the edges of the distributions 'point' unambiguously towards the exact endpoints. If the shape of a distribution is sufficiently concave at high values, the endpoint will most likely be underestimated and large systematic uncertainties must be added. In general the shapes of the mass distributions vary if the sparticle masses are varied. To investigate the range of possible shapes for each distribution, the full cascade was generated for approximately 500 unique mass scenarios, and the resulting theoretical mass distributions studied visually.

A representative selection of mass scenarios, showing some of the shape variety of the gluino distributions, is given in figure 1. In generating these decays, quarks and leptons are assumed to be massless, which in the worst case (b-quark) leads to a perfectly acceptable error of $\mathcal{O}$(MeV). Furthermore, only decay phase space has been used, without the associated matrix elements. In principle, this ignores possible spin correlations between leptons and/or quarks. However, since the distributions used here are summed over lepton charge, no spin effects are expected [16]. A similar investigation for the squark distributions was performed in [12]. See also [17].

Since m_{qq} is constructed from two nearest neighbours in the decay chain, the shape is triangular for any masses, similar to m_{ll}. Its endpoint can thus in principle be determined quite accurately. The shape of the m_{qqll} distribution depends on the masses, but in practically all scenarios the edge is well described by a linear descent towards the theoretical endpoint. This should guarantee its determination experimentally if the background is sufficiently low. For most scenarios this is also true for $m_{qql(\text{low})}$, although the distribution can take on other shapes.

The three 'high' distributions, $m_{qql(\text{high})}$, $m_{q_{\text{f}}l(\text{high})}$ and $m_{q_{\text{n}}l(\text{high})}$, show a large variety of forms. The available shapes of the $m_{q_{\text{f}}l(\text{high})}$ distribution are very similar to those of the $m_{q_{\text{n}}l(\text{high})}$ distribution and are not reproduced here (see [12]). A common feature of these distributions is the danger of not noticing the 'foot', seen, for example, in $m_{qql(\text{high})}$, scenario (iv), where the true maximum value may be obscured by backgrounds.

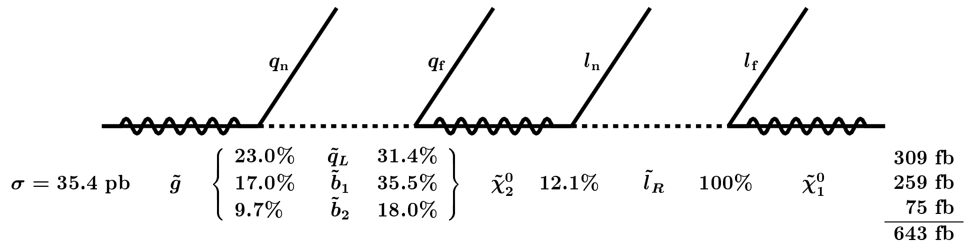

Figure 2: SPS 1a cascade decay with branching ratios and cross-sections.

The last of the three-particle distributions, $m_{q_n ll}$, also has an extensive variety of shapes. The behaviour of the edge is usually reasonable, but with a certain danger of foot-like structures, as in scenario (i). Finally, the two $m_{q_n l}$ distributions are often unreliable in that the edges are concave. It may therefore be difficult to get good estimates of the endpoints.

In summary, from the 500 mass scenarios of which the distributions in figure 1 comprise a fairly representative selection, the following can be stated regarding their overall behaviour: The distributions m_{qq} and m_{qqll} point reliably towards the endpoint for any mass scenario. Somewhat less reliable are the endpoint estimates found from the three-particle distributions. Lastly, even less reliable endpoint estimates can be obtained from the two $m_{q_n l}$ distributions. In the next section we will see how these statements change for a 'realistic' experimental setup.

3. Measuring gluino endpoints for SPS 1a

Here we investigate the measurement of the endpoints associated with gluino decays for SPS 1a at ATLAS. Unless otherwise stated, the details of the analysis are identical to those for the squark chain, as described in ref. [12], and will not be reproduced here.

3.1 Signal and backgrounds

The SPS 1a point is defined by the mSUGRA GUT-scale parameter values

$$m_{1/2} = 250\,\text{GeV}\,, \qquad m_0 = -A_0 = 100\,\text{GeV}\,, \qquad \tan\beta = 10\,, \qquad \mu > 0 \tag{3.1}$$

evolved down to the electroweak scale by version 7.58 of `ISAJET` [18]. The masses of particles at the electroweak scale can be found in [12]. Figure 2 shows the signal chain with branching ratios: to the left the production rate of gluinos is shown, followed by the branching ratios of a gluino into left-handed squarks and both sbottom states. Since the mass difference between $\tilde{b}_1$ and the other squarks is comparable to the mass difference between the gluino and the squarks, phase space effects become significant, resulting in a noticeably enhanced decay rate into $\tilde{b}_1$.

Signal and background are generated for 300 fb^{-1}, which corresponds to three years at design luminosity of 10^{34} cm^{-2}s^{-1}. The low-energy parameters are passed, via the standard interface, to PYTHIA 6.2 [19] which calculates the decay widths and the LHC cross-sections by use of CTEQ 5L [20] PDF's, and generates the events. Finally ATLFAST 2.60 [21] performs a parametrised fast simulation of the ATLAS detector. The simulation setup is identical to that used for the squark-endpoint analysis, except that four jets are now required with $p_T^{\text{jet}} > 150, 100, 50, 20\,\text{GeV}$, rather than only three. Also, the definition of M_{eff} is extended to include the fourth jet.

The QCD background is cut away by the requirement of two leptons[2] and of considerable missing p_T. For the processes involving Z and W the requirement of high hadronic activity together with the missing p_T removes nearly all events. After these rather hard cuts, the Standard Model background consists of approximately 95% $t\bar{t}$. Most likely the Standard Model background is significantly underestimated, as the parton shower approach of PYTHIA does not generate at a realistic rate the hard jets which are required in the selection cuts. However, because of the large SUSY cross-section for this scenario, the main background will come from other SUSY processes. The possible underestimation of the Standard Model background is therefore not a danger for the current analysis.

It is convenient to divide the background into three different parts, 'lepton-uncorrelated', 'lepton-correlated' and 'combinatorial'. The two first consist of events which do not contain the signal chain. In the *lepton-uncorrelated* background two leptons are produced, but in different parts of the decay and therefore independently. With the assumption of lepton universality and neglecting the mass difference between electrons and muons, which is very reasonable for the energies involved, this background can be removed by subtracting the distribution for different-flavour leptons, as was done in ref. [12].

For the *lepton-correlated* background, the leptons are always same-flavour, so no different-flavour sample is available to show its distribution. These events typically come from the decay of Z, in which case they can to some degree be controlled, or from sleptonic decay of neutralinos. In the latter case no particular signature, e.g. in the m_{ll} distribution, is available to discriminate this background from the signal. In particular much of this background will come from $\tilde{\chi}_2^0$'s decaying sleptonically, but which are not part of our signal chain. For the analysis of the squark chain, as done in [12], one important criterion is that the $\tilde{\chi}_2^0$'s produced from squarks make up a good fraction of the total $\tilde{\chi}_2^0$ production. Events with $\tilde{\chi}_2^0$'s not originating from the relevant squarks usually still contain jets and constitute a large part of the background. As the signal chain grows longer, this background increases relative to the signal. In the case of the whole gluino chain what is important is that the $\tilde{\chi}_2^0$'s with a gluino grandparent are not severely outnumbered by the total $\tilde{\chi}_2^0$ production, for the events selected. This is a stricter criterion, and we will find that the flavour of the intermediate squark, whether it is $\tilde{q}_L$ or $\tilde{b}$, will be crucial for the isolation of the signal.

The third background type, combinatorial background, is a result of our inability to know which of the jets correspond to the quark sent out from the gluino (q_{n}) and from the squark (q_{f}). In most analyses one assumes that the quark from a squark decay can on average be distinguished from the quark from a gluino decay on the basis of hardness. In most mSUGRA scenarios this is viable, as $\tilde{\chi}_2^0$ is so much lighter than the squark. Since two

[2]For convenience of notation we will for the rest of the paper use 'lepton'/'slepton' for the two first generations and 'tau'/'stau' for the third generation.

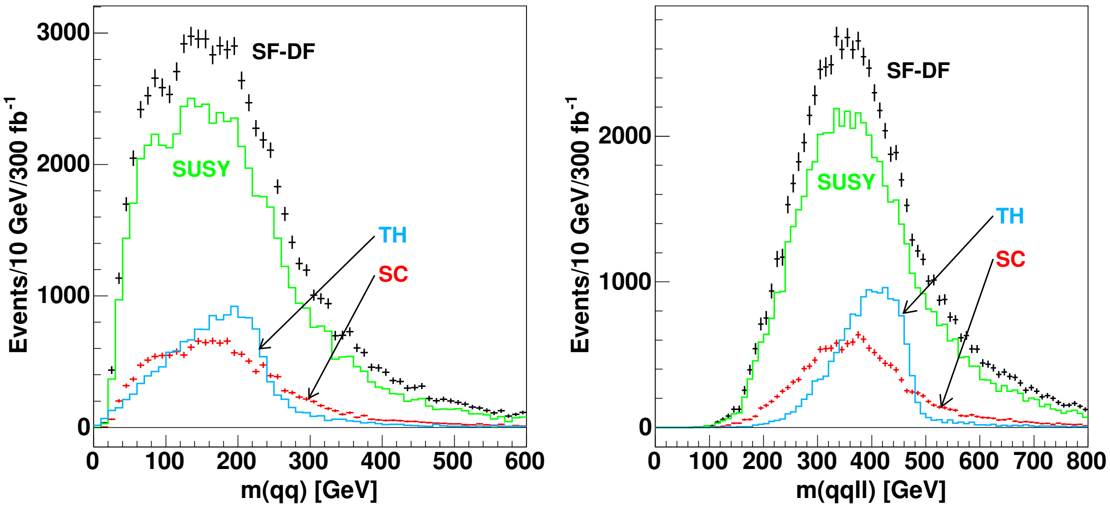

Figure 3: Invariant mass distributions for non-b-tagged events. Endpoints not detectable. See the text for details.

squarks are expected in nearly all events, assuming here $m_{\tilde{g}} > m_{\tilde{q}}$, one can attribute the two hardest jets to the decay of the two squarks. Remaining jets can then be attributed to gluino decays, other quarks in the event, e.g. from the decay of t or W, and/or the underlying event. The exact jet selection algorithms used in this study are based on these assumptions, and will be detailed in the subsections below.

In more general SUSY scenarios it need not be the case that q_{f} is harder than q_{n}. In general, given an unknown SUSY scenario, the appropriate jet selection procedure must be the result of careful study. For this also the mass hierarchy of the gluino and the squarks must be established. A systematic study of how such information can be obtained is lacking but would be very valuable.

3.2 Non-b-tagged distributions

In figure 3 two of the non-b-tagged distributions, m_{qq} and m_{qqll}, are shown. In black with error bars the different-flavour-subtracted distribution ('SF-DF') is shown. Solid green shows the SUSY background ('SUSY'). Its shape is given by the lepton-correlated part, but the lepton-uncorrelated part is also significant and increases the random fluctuations. The Standard Model background is negligible and is not shown separately. The blue curve shows the parton-level distribution of the selected events ('TH'), while the red points with error bars show the part of the different-flavour-subtracted sample which contains the correct signal chain ('SC'), also referred to as the 'signal-chain distribution'. Any discrepancy between these two distributions is mostly due to combinatorial background, i.e. from picking the wrong jets.

For these distributions q_{f} was assumed to be one of the two hardest jets while q_{n} was selected among number three or four in p_T-hardness. This is in line with the mass assumptions usually valid in mSUGRA scenarios, as described above. The jet selection used for the distributions plotted was, on an event-by-event basis, the one out of four possible combinations which gave the smallest m_{qqll} value. In addition we required that neither of the involved jets was b-tagged. (The b-tagging simulation is described in [12] and is rather crude, although with a reasonable overall behaviour.)

It is clear that the positions of the endpoints, which are seen in the parton-level distributions ('TH'), are not easily detectable from the different-flavour-subtracted sample. This is mainly due to the size of the lepton-correlated part of the SUSY background ('SUSY'), which makes up $\sim 80\%$ of the total sample. Structures in the signal part of the sample are therefore not easily identified. This result can be anticipated from of [12, table 3], which shows that only $8.2/32.8 = 25\%$ of $\tilde{q}_L$'s originate from a gluino. The ratio of gluino-induced $\tilde{\chi}_2^0$'s becomes therefore quite small.

Another difficulty is the combinatorial background. The signal-chain distributions ('SC') do not at all point to the nominal endpoints at 242 GeV and 490 GeV (for $\tilde{u}_L$). This is because the jet pair selected is often not the correct one.

Other jet selection algorithms of this simple type have been tried, but none allows any edge structure caused by the kinematics of the decay chain to be recognised. This is also true for the other five gluino distributions (not shown). One must therefore conclude that the endpoints of the non-b-tagged gluino distributions are not experimentally obtainable by looking at one distribution at a time. If instead correlations between mass distributions were investigated it might be possible to identify endpoint-related edge structures.

3.3 b-tagged distributions

The distributions of the b-tagged samples are shown in figures 4–5. The curves follow the colour code of figure 3, except the Standard Model background ('SM') is also shown (green points with error bars). For the b-tagged distributions the different-flavour distribution is $\sim 40\%$ of the same-flavour distribution, which is somewhat larger than for the non-b-tagged distribution where the ratio is $\sim 25\%$. In both cases the different-flavour distribution favours lower mass values and does not interfere very much with the edge structure.

Contrary to the previous case, the b-tagged distributions have clear edge structures which provide values for the endpoints. The main reason for this is that the different-flavour-subtracted SUSY background (solid green) now makes up a manageable 35%, to be compared with 80% for the non-b-tagged sample. This reduction is due to the fact that *the majority of $\tilde{b}$'s are produced indirectly from gluino decay* (because of the low b-content of the proton) in combination with a jet selection requirement of exactly two b-tagged jets. Although the total production of $\tilde{\chi}_2^0$ is 6–7 times larger (see figure 2 and [12, table 3]) than the production which starts out from $\tilde{g} \to \tilde{b}b$, two b-jets are also needed, which reduces considerably the number of selected background events. (For background events the b's are usually produced in the other chain, typically from the same $\tilde{g} \to \tilde{b}b$ which then does not continue sleptonically, or from $\tilde{g} \to \tilde{t}_1 t$ in either of the chains, which also produces multiple b's.) Since the rate of b-jets is considerably smaller than the rate of light jets, also in SUSY events, we are likely not to have additional b-jets in a signal event. The combinatorial background is therefore small, as is clear from the good correspondence between the parton-level distribution ('TH') and the signal-chain distribution ('SC').

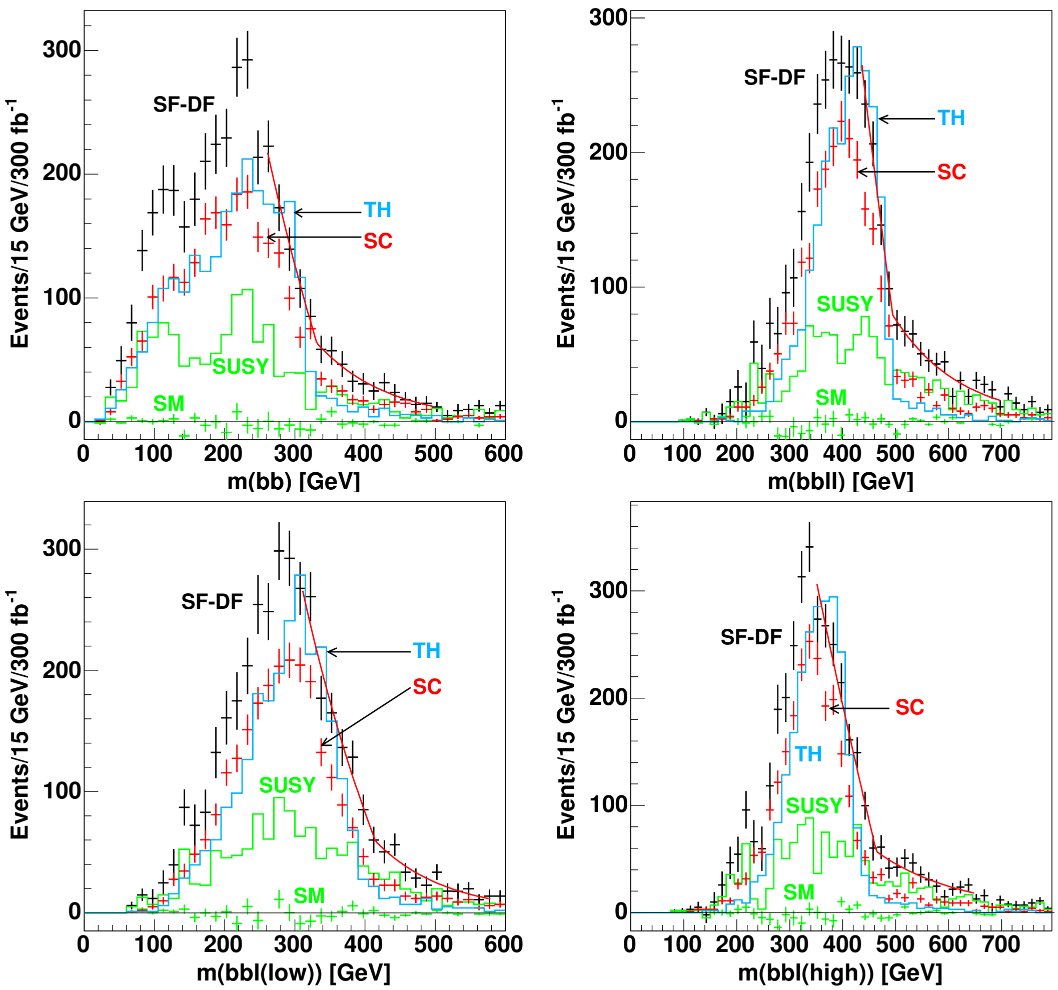

Figure 4: Four good b-tagged invariant mass distributions. See the text for details.

The specific jet-selection used here is in line with the previous assumption that $b_{\rm f}$ is harder than $b_{\rm n}$. The first is searched for among the two p_T-hardest, the second among number three and four. Only events which have one b-jet among the two hardest and one among the two next were selected. (In a more realistic study where emphasis is put on issues like fitting techniques, impact on the distributions from the precuts etc., it would be natural to investigate the effect of also including events which have their two b-tagged jets as number 1 and 2 or as number 3 and 4.)

For the distributions in figure 5 no endpoint estimation is attempted. The two $m_{b_{\rm n}l}$ distributions are distrusted since they do not usually 'point' towards the maximum value, as shown in figure 1. The phase space corresponding to the largest values is very small, leaving only an experimentally undetectable tail to mark the endpoint. These distributions are furthermore made less useful by the need to distinguish $b_{\rm n}$ from $b_{\rm f}$. For the distributions of figure 4 this is not an issue because both b's were used. At SPS 1a the endpoints involving $b_{\rm n}$ have smaller nominal values than the corresponding endpoints with $b_{\rm f}$. Consequently, if we are not able to cleanly distinguish $b_{\rm n}$ from $b_{\rm f}$, all distributions which have $b_{\rm n}$ as

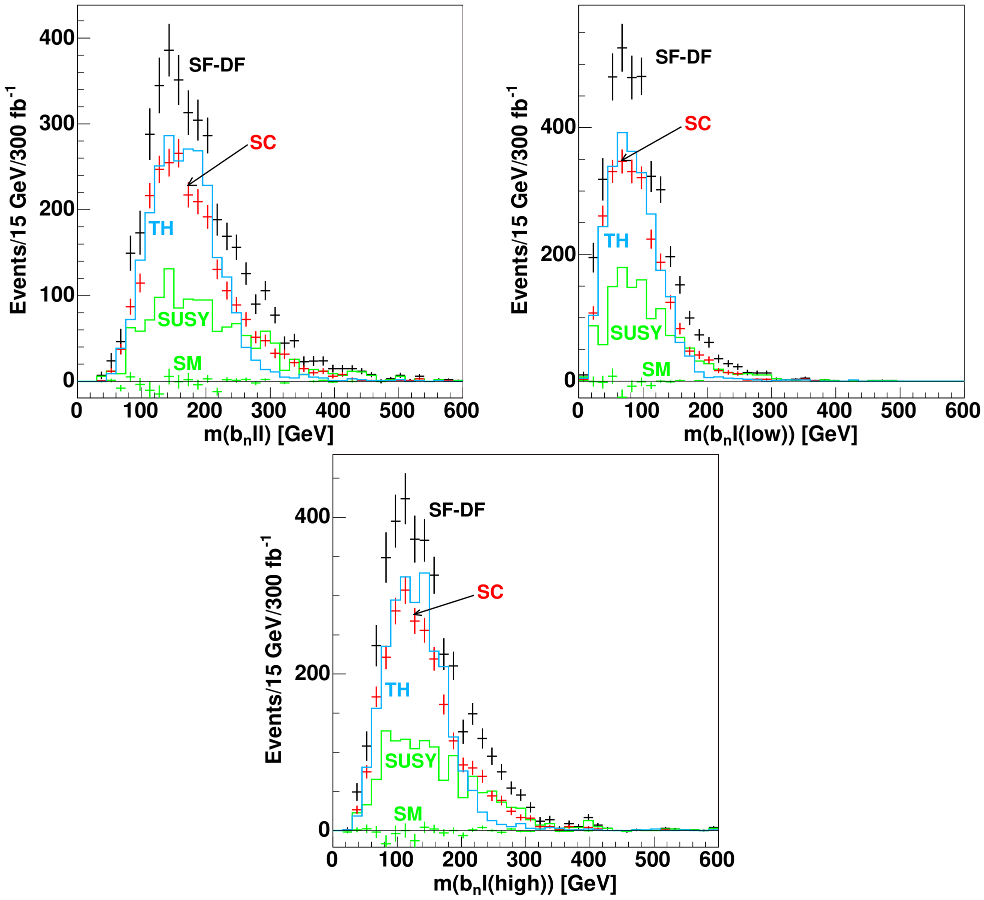

Figure 5: Three bad b-tagged invariant mass distributions. See the text for details.

the only quark will get a contamination which stretches beyond the endpoints. If this contamination is substantial, and here it is, the $b_{\rm n}$ endpoints will be washed out. The combination of these two effects seems to disable these three distributions. The nominal endpoints are $m_{b_{\rm n}ll}^{\rm max} = 281$ GeV, $m_{b_{\rm n}l(\rm low)}^{\rm max} = 197$ GeV and $m_{b_{\rm n}l(\rm high)}^{\rm max} = 248$ GeV, which are clearly not obtainable from the distributions in figure 5. To cope with the problem of distinguishing $b_{\rm n}$ and $b_{\rm f}$ more general distributions could be constructed, as was discussed in section 2.2.

For m_{bb} the fit values are a considerable 25 GeV higher than the nominal value, and are not really accounted for by the errors. It is not completely understood why the discrepancy is so large; whether it is a statistical fluctuation or some other effect. Since the reconstruction resolution is much worse for jets than for leptons, one should expect that a mass distribution constructed from jets alone will be more smeared and therefore give worse endpoint determination than one which also involves leptons. This is probably part of the reason.

To extract the endpoints from the distribution, signal and background hypotheses are needed. Usually, at this level of detail, a straight line is used for the signal in the edge region. We see from the theory distribution of figure 1 that the straight-line hypothesis in the edge region is normally quite well supported for the four distributions of figure 4. (The exception is $m_{qql(\text{high})}$, which in some cases might have a dangerous foot at the very last part of the edge.)

Which background hypothesis to use is less clear. The background is here mainly from other SUSY processes, and therefore in principle unknown. One attempt to sketch the shape of the background, is by combining the lepton and the jet sectors of different events into a mixed-event sample, as described in [12, section 5]. The shapes of the mixed-event distributions are then used as background hypotheses. Another way is to simply select for the background some appropriate function, based on the distribution slightly beyond the edge, where only background resides. An exponential or a polynomial usually gives a fair description. Whatever the signal and background hypotheses, systematics are introduced which may not always be easy to estimate.

For the plots of figure 4 the signal was fitted with a straight line, while the background was modeled by both an exponential and a mixed-event sample. A four/three-parameter fit was then performed by use of MINUIT [22] for exponential/mixed-event background hypothesis and several different histogram binnings and fit ranges. Each distribution gives fit values and statistical errors within a fairly narrow interval, indicative of the systematic uncertainty in the fitting procedure. The results of the fits are summarised in table 1 at the end of this section, after the discussion of energy scale errors.

3.4 Propagation of energy scale errors

In ATLAS it is expected that the absolute energy scale of jets and leptons will be known to 1% and 0.1%, respectively, see [23, chapter 12]. This energy scale uncertainty translates into an uncertainty, or 'error', for any mass constructed from jets and/or leptons. In particular, the masses which go into our distributions have such an error in addition to the statistical error.

Invariant masses which are constructed from jets alone or leptons alone, will inherit their uncertainties of 1% or 0.1%, respectively. For an invariant mass made from one lepton and one jet, the energy scale error is at 0.5%. For masses constructed from more than two jets and leptons, the energy scale error is not constant, but varies within a given calculable interval, depending on whether it is the jet(s) or the lepton(s) which dominate the invariant mass for the given event.

To find appropriate energy scale errors, we must investigate m_{qqll}, m_{qql} and m_{qll}. The overall masses can be expressed in terms of two-particle masses, which have a constant energy scale error:

$$m^2_{qqll} = m^2_{qq} + m^2_{q_\mathrm{n}l_\mathrm{n}} + m^2_{q_\mathrm{n}l_\mathrm{f}} + m^2_{q_\mathrm{f}l_\mathrm{n}} + m^2_{q_\mathrm{f}l_\mathrm{f}} + m^2_{ll} \tag{3.2}$$

$$m^2_{qql} = m^2_{qq} + m^2_{q_\mathrm{n}l} + m^2_{q_\mathrm{f}l} \tag{3.3}$$

$$m^2_{qll} = m^2_{ql_\mathrm{n}} + m^2_{ql_\mathrm{f}} + m^2_{ll}\,. \tag{3.4}$$

Absolute lower/upper limits for the energy scale error of the quantities on the left-hand side can then be found by assuming that the right-hand side is totally dominated by the

Edge	Nominal Value [GeV]	Fit Value [GeV]	Energy Scale Error (σ^{scale}) [GeV]	Statistical Error (σ^{stat}) [GeV]
$m_{bb}^{\max}$	312.7	335–339	3.4	6–10
$m_{bbll}^{\max}$	496.3	494–500	3.3	5–7
$m_{bbl(\text{low})}^{\max}$	413.2	407–417	3.3	8–12
$m_{bbl(\text{high})}^{\max}$	461.9	454–462	3.3	5–7

Table 1: Endpoint values found from fitting the edges in figure 4, for 300 fb^{-1}. The nominal values correspond to the mass of $\tilde{b}_1$ which is produced at significantly higher rates than the heavier $\tilde{b}_2$. The energy scale errors are based on the discussion in section 3.4. No values are given for the three distributions in figure 5.

term which has the smallest/largest energy scale error. This results in

$$\frac{\sigma(m_{qqll})}{m_{qqll}} \in (0.1, 1)\%\,, \qquad \frac{\sigma(m_{qql})}{m_{qql}} \in (0.5, 1)\%\,, \qquad \frac{\sigma(m_{qll})}{m_{qll}} \in (0.1, 0.5)\%\,, \tag{3.5}$$

where σ denotes the energy scale error. These are absolute limits valid for any mass scenario. To find the relevant numbers for SPS 1a, all accepted events were reexamined; scaling the jet momenta of each event by 1.01 and taking the ratio of the new and the old invariant mass. We then find the following average and root-mean-square values (in parentheses) of the relevant energy scale errors,

$$\begin{aligned} \frac{\sigma(m_{bbll})}{m_{bbll}} &= 0.66(0.10)\%\,, \qquad & \frac{\sigma(m_{bbl(\text{low})})}{m_{bbl(\text{low})}} &= 0.80(0.11)\% \\ \frac{\sigma(m_{bbl(\text{high})})}{m_{bbl(\text{high})}} &= 0.71(0.10)\%\,, \qquad & \frac{\sigma(m_{b_{\rm n}ll})}{m_{b_{\rm n}ll}} &= 0.42(0.02)\% \end{aligned} \tag{3.6}$$

Inclusion of the lepton energy scale will give a small correction to these numbers. For $m_{b_{\rm n}ll}$, which we will not be using, the energy scale is nearly constant. For the three other distributions, the errors lie between approximately 0.5% and 1%, and fairly uniformly distributed, as is reflected in the root-mean-square values. For the fitting, only the energy scale error for masses which lie in the edge region is relevant. However, it turns out that at SPS 1a and for these distributions, the error is almost the same for low as for high invariant mass values. Although the error of each distribution is found to lie in a fairly broad interval rather than being constant for all events, we have here used the average values, eq. (3.6), as a basis for the energy scale errors in table 1.

An alternative approach could be to scale the jet momenta up/down as done above, then redo the entire fitting process on the new distributions and from this extract the effect of the energy scale error. For this to work one would have to disentangle the effect of the scaling from the yet uncontrolled systematics of the fitting procedure. At the present stage of fitting competence the gain from using a more correct procedure is probably lost in the increased complexity.

JHEP06(2005)015

4. Masses from endpoints

4.1 10,000 ATLAS experiments

The sparticle masses can be obtained from a numerical fit based on the gluino endpoints found in the previous section together with the squark endpoints of [12]. Due to the simplistic treatment of the detector effects and the endpoint fitting, we do not trust the fit values to be representative of what a more complete simulation would give. Therefore, rather than use directly the endpoint values obtained from the distributions, we generate an ensemble of 10,000 ATLAS experiments based on the estimated *errors*, as done in [10].

For each experiment the endpoint values $\mathbf{E}^{\rm exp}$ are combined with the general endpoint expressions $\mathbf{E}^{\rm th}$ in a least-square function Σ,

$$\Sigma = \left[\mathbf{E}^{\rm exp} - \mathbf{E}^{\rm th}(\mathbf{m})\right]^T \mathbf{W} \left[\mathbf{E}^{\rm exp} - \mathbf{E}^{\rm th}(\mathbf{m})\right]. \tag{4.1}$$

The weight matrix $\mathbf{W}$ is the inverse of the covariance matrix which is constructed from the endpoint errors and appropriately handles the endpoint correlations due to the energy scale error. The minimisation of Σ then yields the masses. Due to the composite nature of the endpoint expressions, there are usually several competing Σ minima for a given set of endpoints. If these minima are close in Σ value, they must all be considered, opening the way for multiple mass solutions. Finally, ensemble distributions for the masses can be plotted and studied, and are to be interpreted as probability distributions for the masses which can be obtained at the LHC. We will be interested in the mean and width of these ensemble distributions. For more details of the procedure, see [12].

4.2 Mass estimation

In total six sparticles are involved in our decay chains: $\tilde{\chi}_1^0$, $\tilde{l}_R$, $\tilde{\chi}_2^0$, $\tilde{q}_L$, $\tilde{b}_1$ and $\tilde{g}$. The masses of the first five of these could already be obtained from the squark endpoints alone, as was done in [12]. The gluino mass is accessed by the gluino endpoints. Since these also involve the other masses (except $m_{\tilde{q}_L}$), the squark endpoints and the gluino endpoints are combined in a single fit where all the masses are free parameters. The six squark-endpoint measurements are given in [12, table 4 (upper part)]. The values of the right-most column, 'Syst. Fit Error' are not used. For the gluino endpoints of table 1 (in the present paper) the statistical errors are given as intervals. We take here the midpoints of the intervals, and further assume that the systematics of the fit values (also given by intervals) will be settled, or at least dominated by the statistical errors. This assumption might be somewhat optimistic, and should be kept in mind when contemplating the results obtained below. (In the next section we will look at the effects of doubling the errors.) Furthermore, we decided to use only three out of seven gluino distributions. In particular the choice of excluding $m_{bb}^{\rm max}$ was made after consultation with the Monte Carlo truth at our specific SUSY scenario, which is not a viable strategy in a realistic setting. More study could however promote this result into a generic one.

If we start from the squark endpoints and add only *one* of the gluino endpoints in the numerical fit, the gluino mass will be determined and all the other masses will remain unchanged. This is so because there is exactly one new measurement for one new mass.

JHEP06(2005)015

The gluino mass returned from the fit is the one which gives zero for the new terms added to Σ, so there is no increase in the Σ-value. Also, the number of minima remains unchanged by adding one more measurement for one more mass. This situation is similar to the determination of $m_{\tilde{b}_1}$ in [12]. Only one endpoint involves $\tilde{b}_1$, so its inclusion has no effect on the other masses or number of minima.

When more gluino endpoints are added, the gluino sector becomes over-determined, and the positions of the minima will change, i.e. the other masses will be affected. Since the gluino endpoints have somewhat larger errors than the squark endpoints, large effects are not expected, except perhaps for $\tilde{b}_1$. Below, results are given for the case when all three selected gluino endpoints are used.

For the current precision of the endpoint measurements, the numerical fit nearly always returns two minima, one in mass region *(1,1)*,[3] which is the region of the nominal masses at SPS 1a, and one in mass region *(1,2)*. If the minima are close in Σ-value, both must be considered. Table 2 shows the probability of having more than one solution in an experiment. The cut on $\Delta\Sigma$, the distance to the global minimum, gives the quality of the second minimum. In most cases the *(1,1)* minimum is the selected one. These numbers are very similar to the numbers obtained without the gluino endpoints, [12, table 5], where a more detailed description can also be found.

	# Minima	*(1,1)*	*(1,2)*
$\Delta\Sigma = 0$	1.00	91%	9%
$\Delta\Sigma \leq 1$	1.11	95%	16%
$\Delta\Sigma \leq 3$	1.30	98%	32%
$\Delta\Sigma \leq 99$	1.87	99%	87%

Table 2: Number of minima for various $\Delta\Sigma$ cuts and their whereabouts.

The masses are given in table 3 for minima which satisfy $\Delta\Sigma \leq 1$. The numbers are very close to the ones obtained without the gluino endpoints, see [12, table 6]. Only $\tilde{b}_1$ is affected, as was expected.

The gluino mass is quite well determined. The ensemble mean is at the nominal value, and the root-mean-square deviation from the mean is 7.2 GeV, only a GeV more than for $m_{\tilde{q}_L}$. For the other masses, especially the lighter ones, mass differences are much more accurately determined than the masses themselves. This is also the case for the gluino, although to a lesser degree, as is seen from the smaller root-mean-square value for $m_{\tilde{g}} - m_{\tilde{\chi}_1^0}$ of 5.6/5.4 GeV. When the correlation to $\tilde{\chi}_1^0$ is taken into account, as in mass differences, $\tilde{q}_L$ is better determined than $\tilde{g}$, as it naively should be from the smaller squark endpoint errors. Since the gluino endpoints involve the sbottom mass, one might expect that the masses of $\tilde{g}$ and $\tilde{b}_1$ have a considerable correlation. Some correlation is found, as can be seen from comparing the root-mean-square value of $m_{\tilde{g}} - m_{\tilde{b}_1}$ with that of $m_{\tilde{b}_1}$ alone.

The ensemble distributions summarised in table 3, i.e. for $\Delta\Sigma \leq 1$, are shown in figure 6. The unfilled distributions in black show from left to right $m_{\tilde{\chi}_1^0}$, $m_{\tilde{l}_R}$, $m_{\tilde{\chi}_2^0}$, $m_{\tilde{b}_1}$, $m_{\tilde{q}_L}$ and $m_{\tilde{g}}$ for solutions in the nominal region *(1,1)*. We will have such a solution in 95% of the experiments, see table 2. The unfilled distributions in blue (grey) show the same masses for solutions in region *(1,2)*. Such a solution occurs in 16% of the experiments. (For

[3] The definition of the regions is given in [12, section 4.3]. For a mass region *(i,j)* the first index refers to the expression used for $m_{q_f ll}^{\max}$, the second index shows which combination is used for $(m_{q_f l(\mathrm{low})}^{\max}, m_{q_f l(\mathrm{high})}^{\max})$, see [12, eqs. (4.4)–(4.5)].

		(1,1)		*(1,2)*	
	Nom	Mean	RMS	Mean	RMS
$m_{\tilde{\chi}_1^0}$	96.1	96.3	3.7	85.5	3.4
$m_{\tilde{l}_R}$	143.0	143.2	3.7	130.6	3.8
$m_{\tilde{\chi}_2^0}$	176.8	177.0	3.6	165.7	3.5
$m_{\tilde{q}_L}$	537.2	537.5	6.0	523.5	5.0
$m_{\tilde{b}_1}$	491.9	492.2	12.5	471.8	12.6
$m_{\tilde{g}}$	595.2	595.5	7.2	582.5	6.8
$m_{\tilde{l}_R} - m_{\tilde{\chi}_1^0}$	46.92	46.93	0.28	45.11	0.72
$m_{\tilde{\chi}_2^0} - m_{\tilde{\chi}_1^0}$	80.77	80.77	0.18	80.19	0.29
$m_{\tilde{q}_L} - m_{\tilde{\chi}_1^0}$	441.2	441.2	3.1	438.0	2.8
$m_{\tilde{b}_1} - m_{\tilde{\chi}_1^0}$	395.9	396.0	11.2	386.3	11.2
$m_{\tilde{g}} - m_{\tilde{\chi}_1^0}$	499.1	499.2	5.6	497.0	5.4
$m_{\tilde{g}} - m_{\tilde{b}_1}$	103.3	103.3	9.1	110.7	9.5

Table 3: Masses (Mean) and root-mean-square deviations from the mean (RMS) of minima in regions *(1,1)* and *(1,2)*, for $\Delta\Sigma \leq 1$. The nominal masses (Nom) are given in the second column. All values in GeV. See the text for more details.

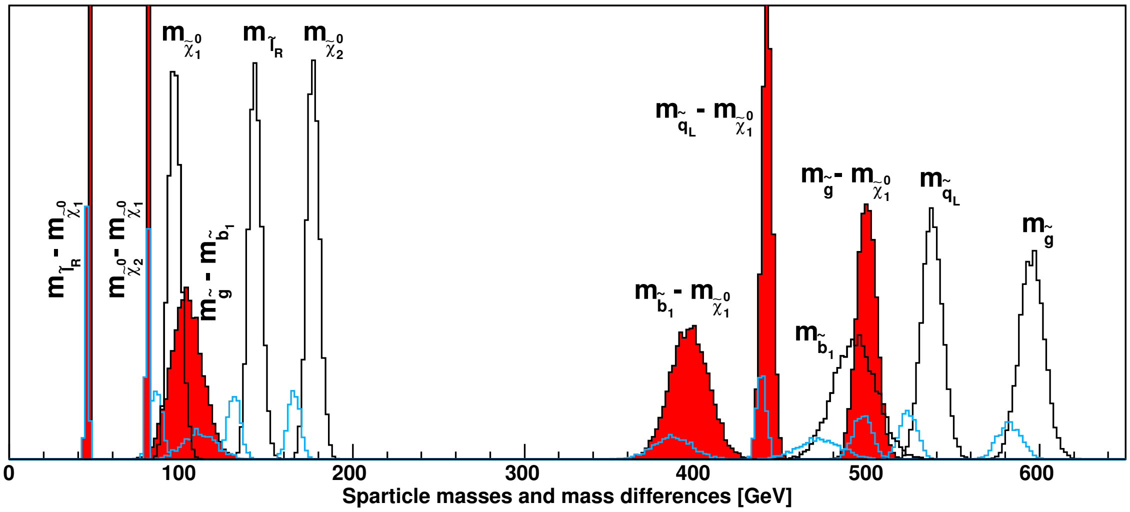

Figure 6: Sparticle masses and mass differences for solutions with $\Delta\Sigma \leq 1$. See the text for details.

$\Delta\Sigma \leq 1$ there is an 11% chance of having both solution types.) The smaller rate of the *(1,2)* solutions is reflected in the smaller area under the blue curves. The *(1,2)* solutions return slightly lower masses, so these distributions are positioned 'down' (due to the lower rate) and slightly to the left of the *(1,1)* distributions. The filled distributions show from left to right $m_{\tilde{l}_R} - m_{\tilde{\chi}_1^0}$, $m_{\tilde{\chi}_2^0} - m_{\tilde{\chi}_1^0}$, $m_{\tilde{g}} - m_{\tilde{b}_1}$, $m_{\tilde{b}_1} - m_{\tilde{\chi}_1^0}$, $m_{\tilde{q}_L} - m_{\tilde{\chi}_1^0}$ and $m_{\tilde{g}} - m_{\tilde{\chi}_1^0}$. Again, the most populated distributions (black curves) are for solutions in region *(1,1)*, the least populated (blue curves) for *(1,2)* solutions. For mass *differences* there is more overlap between the *(1,1)* and *(1,2)* solutions, in particular for $m_{\tilde{l}_R} - m_{\tilde{\chi}_1^0}$ and $m_{\tilde{\chi}_2^0} - m_{\tilde{\chi}_1^0}$, of which only the lower parts of the distributions are visible. Mass differences are better determined than the masses themselves, reflected here by the narrower distributions of the former. In the case of $\tilde{b}_1$ this effect is clear for $m_{\tilde{g}} - m_{\tilde{b}_1}$, much less so for $m_{\tilde{b}_1} - m_{\tilde{\chi}_1^0}$, which points to the fact that $\tilde{b}_1$ largely decouples from $\tilde{\chi}_1^0$,

4.3 Edge sensitivities

It may seem a puzzle that $m_{\tilde{g}}$ is determined with much higher precision than $m_{\tilde{b}_1}$. Both masses enter the three new gluino endpoints, but $m_{\tilde{b}_1}$ has in addition the $m^{\min}_{b_f ll(\theta>\frac{\pi}{2})}$ measurement. Naively one might therefore expect the $\tilde{b}_1$ mass to be more precisely determined.

In order to better see how masses are constrained by the endpoint formulas, consider the part of the least-square function Σ which involves one given endpoint and one given mass only. For simplicity of argument, assume that the endpoint measurement is at the nominal value, as are the masses. Changing the given mass away from the nominal value by an amount Δm will give an increase of our selected Σ part by

$$\left(\frac{E(m+\Delta m) - E^{\exp}}{\sigma_E}\right)^2 \approx \left(\frac{E(m) + (\partial E/\partial m)\Delta m - E^{\exp}}{\sigma_E}\right)^2 = \left(\frac{(\partial E/\partial m)\Delta m}{\sigma_E}\right)^2 , \quad (4.2)$$

where E is the value of a particular kinematical endpoint. The value of Δm which gives an increase of Σ by 1 (from this term only), is then given by

$$\Delta m = \frac{\sigma_E}{(\partial E/\partial m)} . \quad (4.3)$$

Since the shift in mass also induces changes to other contributions to Σ, the interpretation of Δm is not straight-forward in terms of mass error. Still, Δm does combine the precision of the endpoint, given by the endpoint error σ_E, with the response of the endpoint to the mass, which are the two important quantities. The same relation could be derived in a mathematically more intuitive way,

$$\Delta m = \left(\frac{\partial m}{\partial E}\right) \Delta E = \frac{\sigma_E}{(\partial E/\partial m)} , \quad (4.4)$$

where the endpoint variation ΔE is set equal to the experimental error σ_E.

Inclusion of the endpoint error opens for comparison between different endpoints, even if only in a semi-quantitative way which does not take correlations into account. The importance of the different endpoints in constraining a given mass can then be studied. In table 4, values for $\partial E/\partial m$ and Δm are given for both the squark and the gluino endpoints. For the three gluino endpoints of figure 5, where no fit was made and hence no σ is available, Δm is not given.

These numbers show immediately that the three gluino endpoints included in the numerical fit have a strong sensitivity to the gluino mass, but only a very moderate sensitivity to the sbottom mass. Also $m^{\min}_{b_f ll(\theta>\frac{\pi}{2})}$ is seen not to constrain $m_{\tilde{b}_1}$ too much. If $m^{\max}_{bb}$ could be used or some of the squark endpoints other than $m^{\min}_{b_f ll(\theta>\frac{\pi}{2})}$ (numbers shown only for $m^{\min}_{q_f ll(\theta>\frac{\pi}{2})}$), then $m_{\tilde{b}_1}$ might be determined more accurately. The table can also be used to understand better which of the endpoints are important in constraining each of the lighter masses.

	$\tilde{\chi}_1^0$		$\tilde{l}_R$		$\tilde{\chi}_2^0$		$\tilde{q}_L$		$\tilde{b}_1$		$\tilde{g}$	
	$\frac{\partial E}{\partial m}$	Δm	$\frac{\partial E}{\partial m}$	Δm	$\frac{\partial E}{\partial m}$	Δm	$\frac{\partial E}{\partial m}$	Δm	$\frac{\partial E}{\partial m}$	Δm	$\frac{\partial E}{\partial m}$	Δm
$m_{ll}^{\max}$	-0.7	-0.1	-0.6	-0.2	1.3	0.1	-	-	-	-	-	-
$m_{q_{\rm f}ll}^{\max}$	-1.9	-1.2	-	-	0.7	3.2	0.9	2.6	-	-	-	-
$m_{q_{\rm f}ll(\theta>\frac{\pi}{2})}^{\min}$	-0.8	-3.2	-1.6	-1.5	1.7	1.4	0.4	6.2	-	-	-	-
$m_{q_{\rm f}l({\rm low})}^{\max}$	-	-	-3.9	-0.4	3.0	0.6	0.6	2.8	-	-	-	-
$m_{q_{\rm f}l({\rm high})}^{\max}$	-3.2	-0.7	2.2	1.0	-0.3	-8.2	0.8	2.7	-	-	-	-
$m_{b_{\rm f}ll(\theta>\frac{\pi}{2})}^{\min}$	-0.7	-6.5	-1.5	-3.1	1.5	3.0	-	-	0.4	11.8	-	-
$m_{bb}^{\max}$	-	-	-	-	-0.3	-39.6	-	-	-1.3	-8.1	1.7	6.3
$m_{bbll}^{\max}$	-1.3	-5.2	-	-	0.3	23.4	-	-	-0.1	-65.1	1.0	6.5
$m_{bbl({\rm low})}^{\max}$	-	-	-2.3	-4.5	1.5	6.8	-	-	-0.6	-19.0	1.3	8.4
$m_{bbl({\rm high})}^{\max}$	-2.1	-3.2	1.4	4.7	-0.4	-17.6	-	-	-0.3	-24.5	1.1	6.1
$m_{b_{\rm n}ll}^{\max}$	-1.2	-	-	-	0.7	-	-	-	-1.2	-	1.5	-
$m_{b_{\rm n}l({\rm low})}^{\max}$	-	-	-2.6	-	2.1	-	-	-	-0.9	-	1.0	-
$m_{b_{\rm n}l({\rm high})}^{\max}$	-2.1	-	1.4	-	-	-	-	-	-1.1	-	1.3	-

Table 4: Partial derivatives of endpoints with respect to masses at the nominal mass values. The larger the partial derivative $\partial E/\partial m$ is, the more sensitive the given endpoint is to the given mass. The quantity Δm (GeV) is defined by $\sigma_E/(\partial E/\partial m)$, where σ_E is the combined statistical and energy scale error of the endpoint. Numbers are specific for SPS 1a. See the text for more details.

5. Increasing the errors

In the previous section the uncertainties of sparticle masses were found from the estimated errors of the endpoint measurements. The technique of generating an ensemble of experiments with endpoint measurements spread Gaussian-like around the nominal values sidesteps some of the problems of the crude detector simulation and edge-fitting procedure, as only the estimated statistical errors and energy scale errors are then relevant. However, these are also subject to uncertainties. First, for the statistical errors we used the means of supposedly reasonable intervals obtained from recurrent fits with slight variations in bin width, range of fit and fit functions. Clearly these numbers are tentative. Second, one cannot be certain that the energy scale will actually be known to the precision aimed for.

In this section we will therefore investigate two somewhat more conservative scenarios. First we double the statistical errors of all the endpoints, keeping the energy scale errors at the 'default', i.e. at the values given in table 1 (this paper) and [12, table 4]. Then we keep the statistical errors at the default values and double instead the energy scale errors.

However, in order to better understand the changes this will lead to, we first try to disentangle the impact of the statistical errors from that of the energy scale errors for a simplified version of the default analysis considered in the previous section.

5.1 Disentangling statistical from energy scale errors

A simplified analysis is considered, in which only the four endpoints $m_{ll}^{\max}$, $m_{q_{\rm f}ll}^{\max}$, $m_{q_{\rm f}l({\rm low})}^{\max}$ and $m_{q_{\rm f}l({\rm high})}^{\max}$ are used to obtain the masses of $\tilde{\chi}_1^0$, $\tilde{l}_R$, $\tilde{\chi}_2^0$ and $\tilde{q}_L$. This analysis contains

JHEP06(2005)015

	Only σ^{stat}	Only σ^{scale}	Both
$m_{\tilde{\chi}_1^0}$	3.9	0.10	3.9
$m_{\tilde{l}_R}$	3.9	0.14	3.9
$m_{\tilde{\chi}_2^0}$	3.8	0.18	3.8
$m_{\tilde{q}_L}$	5.9	2.4	6.3
$m_{\tilde{l}_R} - m_{\tilde{\chi}_1^0}$	0.28	0.05	0.28
$m_{\tilde{\chi}_2^0} - m_{\tilde{\chi}_1^0}$	0.16	0.08	0.18
$m_{\tilde{q}_L} - m_{\tilde{\chi}_1^0}$	2.0	2.4	3.1

Table 5: Disentangling statistical from energy scale errors. Root-mean-square values of uncertainties in masses and mass differences (GeV). Only the four basic endpoints have been used.

the main features of the comprehensive one where all the endpoints are used, but is easier to interpret. In particular we can use the inversion formulas [12, eqs. (4.13)–(4.16)] appropriate for region (1,1). Notice in these formulas how the three lightest sparticle masses are proportional to $m_{ll}^{\max}$. Hence, these three masses scale with the lepton energy scale error. Conversely, compare this with their dependence on the three squark endpoints. If these three endpoints have identical relative energy scale errors (which in reality is only approximately true for $m_{q_{\rm f}ll}^{\max}$ — here we have assumed it to be exactly true), then the energy scale errors cancel out for the three lightest masses, as is easily seen by letting each of the squark endpoints be scaled by a factor $(1+\delta)$. Consequently, the impact of the energy scale errors on the three lightest sparticles is equal to the lepton energy scale error, which for most purposes is negligible. For the squark mass, this symmetry is broken, $m_{\tilde{q}_L}$ is not proportional to $m_{ll}^{\max}$, so the other relations do not apply either. The squark mass therefore has a noticeable dependence on the energy scale errors.

In order to quantify the statements just made, an ensemble of ATLAS experiments was constructed in the usual way using the default errors of the four squark endpoints. Table 5 shows the root-mean-square values thus obtained for the four masses and the mass differences. Three cases are shown: only statistical errors, only energy scale errors and combined. Even though the energy scale errors are roughly twice the statistical errors for the endpoints being used ([12, table 4]), the latter clearly dominate the mass errors. Only for combinations involving $m_{\tilde{q}_L}$ do the energy scale errors play a role. For $m_{\tilde{q}_L} - m_{\tilde{\chi}_1^0}$ the impact of the two uncertainties are comparable. Comparison with table 3 shows that the stripped scenario accounts for the main features of the complete scenario to which we return below.

5.2 Doubling the statistical errors

Having established that the statistical errors dominate the errors on the masses, we expect large effects from doubling these errors. Table 6 shows a noticeable increase in the rate of *(1,2)* solutions relative to the nominal *(1,1)* solutions. This is no surprise, as SPS 1a lies very close to the border. Allowing larger errors for the endpoints naturally allows more

	# Minima	*(1,1)*	*(1,2)*
$\Delta\Sigma = 0$	1.00	73%	27%
$\Delta\Sigma \leq 1$	1.24	84%	41%
$\Delta\Sigma \leq 3$	1.47	90%	57%
$\Delta\Sigma \leq 99$	1.87	93%	75%

Table 6: Number of minima for various $\Delta\Sigma$ cuts and their whereabouts. The statistical errors are doubled, compared to table 2.

		(1,1)		*(1,2)*	
	Nom	Mean	RMS	Mean	RMS
$m_{\tilde{\chi}_1^0}$	96.1	97.5	7.2	84.2	6.1
$m_{\tilde{l}_R}$	143.0	144.5	7.0	129.0	6.7
$m_{\tilde{\chi}_2^0}$	176.8	178.3	7.0	164.3	6.2
$m_{\tilde{q}_L}$	537.2	539.3	11.0	522.1	8.7
$m_{\tilde{b}_1}$	491.9	494.4	24.3	468.6	24.0
$m_{\tilde{g}}$	595.2	597.4	12.9	581.1	11.7
$m_{\tilde{l}_R} - m_{\tilde{\chi}_1^0}$	46.92	47.03	0.53	44.72	1.21
$m_{\tilde{\chi}_2^0} - m_{\tilde{\chi}_1^0}$	80.77	80.80	0.32	80.07	0.48
$m_{\tilde{q}_L} - m_{\tilde{\chi}_1^0}$	441.2	441.8	4.4	437.8	3.7
$m_{\tilde{b}_1} - m_{\tilde{\chi}_1^0}$	395.9	396.9	21.9	384.4	21.9
$m_{\tilde{g}} - m_{\tilde{\chi}_1^0}$	499.1	499.9	9.4	496.9	9.0
$m_{\tilde{g}} - m_{\tilde{b}_1}$	103.3	103.0	18.0	112.5	18.9

Table 7: Same as table 3, except for doubled *statistical* errors: Mean and root-mean-square deviations from the mean (RMS) (GeV).

of the *(1,2)* region to be accessed. Furthermore, there is an increase in the number of solutions, which is also reasonable. The 10–15 GeV lower mass values of the *(1,2)* solutions become more troubling as the occurrence of this minimum becomes more frequent.

From table 7 we see that doubling the statistical errors very nearly amounts to doubling the errors on the masses. The exception is mainly $m_{\tilde{q}_L} - m_{\tilde{\chi}_1^0}$ whose error increases less. This effect is explained by the discussion in section 5.1, see table 5, which shows that for this particular mass combination the statistical errors only account for half the total error on the mass difference. For $\tilde{g}$ a pattern similar to, but less pronounced than that of $\tilde{q}_L$ can be seen.

5.3 Doubling the energy scale errors

As already anticipated by the previous discussions, changes in the energy scale errors have only minor effects in the SPS 1a scenario at the given integrated luminosity. The doubling of the energy scale errors does not at all change the number and positions of minima from the default values of table 2.

JHEP06(2005)015

		(1,1)		(1,2)	
	Nom	Mean	RMS	Mean	RMS
$m_{\tilde{\chi}_1^0}$	96.1	96.3	3.7	85.5	3.4
$m_{\tilde{l}_R}$	143.0	143.2	3.7	130.6	3.8
$m_{\tilde{\chi}_2^0}$	176.8	177.0	3.6	165.7	3.5
$m_{\tilde{q}_L}$	537.2	537.3	7.3	523.8	6.4
$m_{\tilde{b}_1}$	491.9	492.1	13.0	472.1	13.1
$m_{\tilde{g}}$	595.2	595.3	9.3	582.9	8.9
$m_{\tilde{l}_R} - m_{\tilde{\chi}_1^0}$	46.92	46.93	0.29	45.11	0.72
$m_{\tilde{\chi}_2^0} - m_{\tilde{\chi}_1^0}$	80.77	80.77	0.22	80.19	0.32
$m_{\tilde{q}_L} - m_{\tilde{\chi}_1^0}$	441.2	441.1	5.1	438.3	4.9
$m_{\tilde{b}_1} - m_{\tilde{\chi}_1^0}$	395.9	395.8	11.8	386.6	11.8
$m_{\tilde{g}} - m_{\tilde{\chi}_1^0}$	499.1	499.0	8.1	497.4	8.1
$m_{\tilde{g}} - m_{\tilde{b}_1}$	103.3	103.2	9.3	110.9	9.8

Table 8: Same as table 3, except for doubled *energy scale* errors: Mean and root-mean-square deviations from the mean (RMS) (GeV).

Furthermore, as is seen from table 8, most masses remain largely unaffected, the exception being combinations involving $m_{\tilde{q}_L}$ and to a lesser extent $m_{\tilde{g}}$, as previously noted. The explanation is the same: For the lighter masses the jet energy scale errors cancel out, leaving only the minimal effect of the lepton scale error. In the case of $m_{\tilde{q}_L}$ it does play a role, although not dominant, giving a slight increase, and for $m_{\tilde{q}_L} - m_{\tilde{\chi}_1^0}$ the impact of the energy scale errors is again significant. The same applies to $m_{\tilde{g}}$ and $m_{\tilde{g}} - m_{\tilde{\chi}_1^0}$.

6. LHC + Linear Collider (LC)

Within the time-frame of the analysis of LHC data, measurements from a Linear Collider may become available. While the LHC is able to measure mass differences at high precision, as documented in the previous sections, a Linear Collider will, due to the much cleaner environment, provide precise mass measurements of the sparticles which are kinematically accessible, in particular $\tilde{\chi}_1^0$. Such a measurement will be the scale fixer which is lacking in the LHC data, and will in combination with the LHC measurements allow one to also fix the masses of the heavier sparticles not accessible at the Linear Collider.

To estimate the effect of a Linear Collider measurement of $m_{\tilde{\chi}_1^0}$, we add to our least-square function Σ, a term $[(m_{\tilde{\chi}_1^0} - m_{\tilde{\chi}_1^0}^{\rm LC})/\sigma_{m_{\tilde{\chi}_1^0}}^{\rm LC}]^2$, where the quantity with superscript 'LC' is the Linear Collider measurement, and generate an ensemble of LHC and LC experiments. Since $\sigma_{m_{\tilde{\chi}_1^0}}^{\rm LC} = 0.05\,{\rm GeV}$ [24], the LC measurement practically fixes $m_{\tilde{\chi}_1^0}$ at the nominal value. (For the LHC measurements we use in this section the default endpoint errors.)

For the *(1,2)* solutions, which normally return $\tilde{\chi}_1^0$ masses some 10 GeV below the nominal value, the LC measurement has the dramatic effect of reducing their occurrences to $\sim 1\%$ (for $\Delta\Sigma \leq 3$). These minima can therefore for most purposes be neglected. As a consequence, the probability of having two minima is strongly reduced, to the per mille level. For SPS 1a the Linear Collider measurement thus closes the issue of multiple minima altogether. (This behaviour was already reported in [12], the inclusion of the gluino endpoints thus makes no difference in this respect.)

The combined LHC + LC results are shown in table 9. Comparison with the numbers of table 3 shows that the precision of the mass determination improves considerably when the LC measurement is included. The root-mean-square values of the masses are now approximately equal to the root-mean-square values of mass differences without the LC measurement. For $m_{\tilde{b}_1}$ the correlation to $m_{\tilde{\chi}_1^0}$ is not dominant. The spread of $m_{\tilde{b}_1}$ is therefore still larger than the spread of $m_{\tilde{g}} - m_{\tilde{b}_1}$, which does not feel the fixing of $m_{\tilde{\chi}_1^0}$. As was the case without the LC measurement, the inclusion of the gluino endpoints in the numerical fit does not affect the other masses. The exception is $m_{\tilde{b}_1}$, for which the root-mean-square value is reduced by $\sim 1\,\mathrm{GeV}$ compared to the results in [12].

		(1,1)	
	Nom	Mean	RMS
$m_{\tilde{\chi}_1^0}$	96.05	96.05	0.05
$m_{\tilde{l}_R}$	142.97	142.97	0.29
$m_{\tilde{\chi}_2^0}$	176.82	176.82	0.17
$m_{\tilde{q}_L}$	537.2	537.2	2.5
$m_{\tilde{b}_1}$	491.9	491.9	10.9
$m_{\tilde{g}}$	595.2	595.2	5.5
$m_{\tilde{g}} - m_{\tilde{b}_1}$	103.3	103.3	9.0

Table 9: Mass values (all in GeV) from LHC+LC. Since the occurrences of *(1,2)* solutions are reduced to $\sim$ 1%, they are left out.

7. Conclusion

In this paper we have extended the endpoint method of obtaining masses in R-parity conserving SUSY scenarios to also include the gluino mass, given the decay chain (1.2). All the gluino endpoints have been calculated. Details of the calculations of $m_{qqll}^{\max}$ and $m_{qql}^{\max}(\mathrm{low})$ are given in the appendices. Theory distributions for the seven new distributions were studied for a selection of mass scenarios, revealing that some of the distributions often have little phase space towards higher masses, making them less useful.

An ATLAS simulation of 300 fb^{-1} was performed for the mSUGRA point SPS 1a. While we were not able to detect the gluino edges in the case of an intermediate first or second-generation squark ($\tilde{q}_L$), edges were found and fitted in the case of an intermediate sbottom. This is due to fact that 80% of the $\tilde{b}$'s come from a gluino, together with the jet selection requirement of having two and only two b-tagged jets, both important background-reducing factors. Not all of the endpoints were used. Energy scale errors were discussed and found to lie in intervals. Yet, they were taken as constants in the analysis.

To estimate the precision with which sparticle masses can be obtained at the LHC, an ensemble of 10,000 'gedanken experiments' were performed, in which for each experiment three of the gluino endpoints were combined with the squark endpoints obtained in [12] in a least-square fit to give the masses. Mass differences are better determined than the masses themselves, a generic feature of the method. Furthermore, one set of endpoint measurements in general corresponds to several sets of masses. The inclusion of the gluino endpoints affects the number of minima and the masses of $\tilde{\chi}_1^0$, $\tilde{l}_R$, $\tilde{\chi}_2^0$ and $\tilde{q}_L$ only minimally.

In the case of $\tilde{b}_1$ there is a noticeable correlation to the gluino. The ensemble distribution of the gluino mass was found to have a root-mean-square value of 7 GeV. The spread for $m_{\tilde{g}} - m_{\tilde{\chi}_1^0}$ was found to be about 1.5 GeV smaller.

Spurred by the lack of significant improvement in the ensemble spread of $m_{\tilde{b}_1}$ compared to the precision obtained for $m_{\tilde{g}}$, even though the new measurements involved both, a sensitivity analysis for all the relevant endpoints was performed. This investigation showed that the three gluino endpoints being used have limited sensitivity to the sbottom mass, thus confirming the different impact they have on the gluino and sbottom masses.

Two alternative error scenarios were investigated, one in which the statistical errors obtained from the fast simulation of SPS 1a were doubled, another in which the energy scale errors were doubled. It was shown that the statistical errors of the endpoints, although smaller in magnitude than the energy scale errors, dominate the error on the masses. Only in a few exceptions, like $m_{\tilde{q}_L} - m_{\tilde{\chi}_1^0}$, do the energy scale errors play a significant role.

Finally the impact of a joint LHC–LC analysis was estimated. The endpoint measurements from the LHC were combined with a Linear Collider measurement for the LSP mass. This essentially fixes the SUSY mass scale. Consequently, in the combined analysis the masses themselves are determined with roughly the same precision as that of mass *differences* determined at the LHC alone. According to a dedicated study [25], the anticipated accuracy will suffice to determine the high-scale mass parameters with a precision ranging from 0.1% for $m_{1/2}$ to 14% for A_0.

A. Calculation of $m_{qqll}^{\max}$

Below we use the calculation of the known squark endpoint $m_{q_f ll}^{\max}$ as an aid to obtain $m_{qqll}^{\max}$. We first follow what may seem to be the most obvious route, then note that while this works fine for $m_{q_f ll}^{\max}$, the increased complexity of having one more particle to consider strongly limits the applicability to $m_{qqll}^{\max}$. An alternative method is then developed by which $m_{qqll}^{\max}$ can be found in a straightforward manner.

A.1 Method 1: by means of angles

In the first method we keep the calculation close to the physical progression of the decay, picking up all decay angles and eventually maximising with respect to these. Figure 7 shows in a stepwise manner the $\tilde{q}_L$ decay chain from which $m_{q_f ll}^{\max}$ is calculated. Start in the rest frame of $\tilde{q}_L$, and align the coordinate system to its decay products. Next, boost to the rest frame of $\tilde{\chi}_2^0$, which decays such that l_n is emitted at an angle α relative to the direction of q_f. Finally, boost to the rest frame of $\tilde{l}_R$, which in turn decays; for a given angle α, $m_{q_f ll}$ is maximised by choosing $\mathbf{p}_{l_f}$ opposite to $\mathbf{p}_{q_f} + \mathbf{p}_{l_n}$ in the rest frame of $\tilde{l}_R$ [giving a planar decay configuration].

The resulting $m_{q_f ll}$ is expressed in terms of the angle α and the four sparticle masses involved. In order to maximise with respect to α, the critical points of this constrained $m_{q_f ll}$ distribution must be sought (and tested if they are maxima or minima). In the part of mass space where no critical point is found, the endpoints of the domain, $\alpha \in [0, \pi]$, must

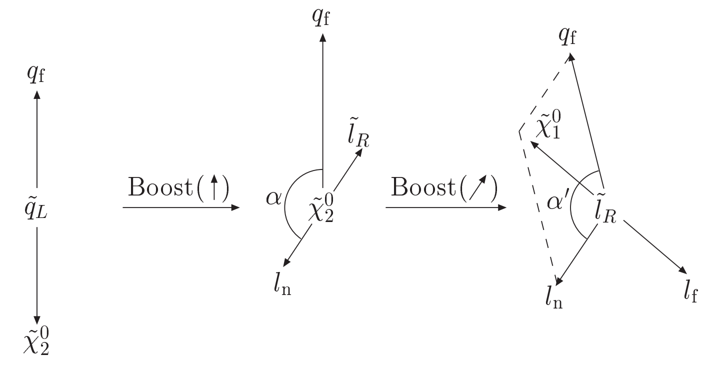

Figure 7: Traditional way of calculating $m_{q_{\mathrm{f}}ll}^{\max}$.

be analysed. In this case, three different expressions are found for three distinct regions in mass space. In total, mass space is thus divided into four regions, each with its specific expression for $m_{q_{\mathrm{f}}ll}^{\max}$, see [12, eq. (4.4)]. (See [11] for a different derivation.)

The above calculation becomes fairly involved, and is preferably performed with the assistance of a computer program. If we now want to calculate $m_{qqll}^{\max}$, a gluino is added at the head of the chain. In general two more angles are needed to describe the gluino decay. However, since the maximum of the endpoint values are obtained with planar decay configurations, one of the angles can be dropped. The remaining additional angle is nevertheless sufficient to complicate significantly the search for extrema of m_{qqll}.

A.2 Method 2: on a line

In the alternative approach to $m_{q_{\mathrm{f}}ll}^{\max}$ (and $m_{qqll}^{\max}$) the physical progression of the decay is not tracked. Instead an expression for the endpoint is found in terms of the one missing four-vector, that of $\tilde{\chi}_1^0$. Arguments which invoke the notion of dominant decays are then applied to point out a number of limiting decay configurations (of great geometrical simplicity) which must be considered.

Investigating first $m_{q_{\mathrm{f}}ll}^{\max}$, the four-vector of the sum of the end products; the two leptons, the quark and the LSP, equals the four-vector of the squark. We therefore have

$$m_{\tilde{q}_L}^2 = (p_{q_{\mathrm{f}}ll} + p_{\tilde{\chi}_1^0})^2 = m_{q_{\mathrm{f}}ll}^2 + m_{\tilde{\chi}_1^0}^2 + 2 p_{q_{\mathrm{f}}ll} \cdot p_{\tilde{\chi}_1^0} \,, \tag{A.1}$$

where $p_{q_{\mathrm{f}}ll}$ is the sum of the four-vectors of the two leptons and the (far) quark. In the rest frame of $\tilde{q}_L$ we have

$$\mathbf{p}_{q_{\mathrm{f}}ll} = -\mathbf{p}_{\tilde{\chi}_1^0} \,, \qquad E_{q_{\mathrm{f}}ll} = m_{\tilde{q}_L} - E_{\tilde{\chi}_1^0} \tag{A.2}$$

which gives

$$m_{q_{\mathrm{f}}ll}^2 = m_{\tilde{q}_L}^2 - m_{\tilde{\chi}_1^0}^2 - 2\left(m_{\tilde{q}_L} \sqrt{m_{\tilde{\chi}_1^0}^2 + \mathbf{p}_{\tilde{\chi}_1^0}^2} - m_{\tilde{\chi}_1^0}^2 \right). \tag{A.3}$$

The smaller the momentum of the LSP is in the rest frame of the initial squark, the larger $m_{q_{\mathrm{f}}ll}$ is, which agrees with one's intuition. At the extreme, if the LSP is brought to rest in the squark rest frame, $m_{q_{\mathrm{f}}ll}$ will attain its largest value, $m_{\tilde{q}_L} - m_{\tilde{\chi}_1^0}$, which corresponds to the critical-point solution of method 1.

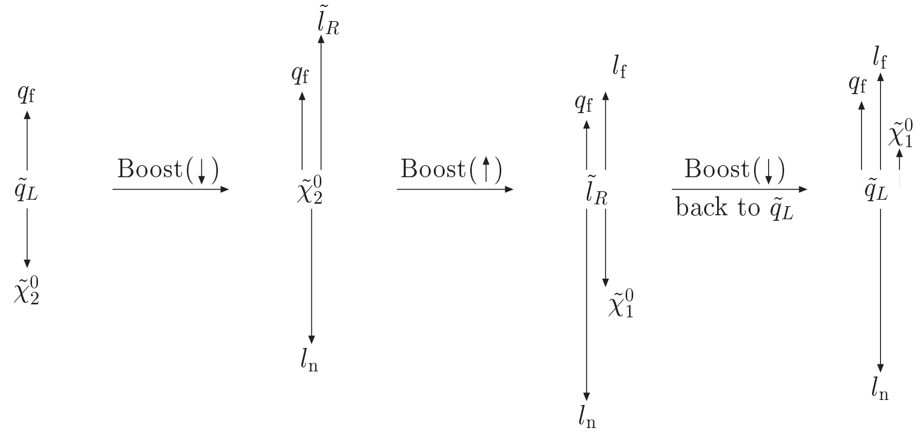

Figure 8: One of three dominance regions for $m_{q_{\rm f}ll}^{\rm max}$

In some regions of mass space it is however not possible to have $\tilde{\chi}_1^0$ at rest in the rest frame of $\tilde{q}_L$. In these regions, one of the intermediate sparticles is sent off with so high momentum that not even optimal choices of directions for the other two decays can bring $\tilde{\chi}_1^0$ to rest (in the rest frame of $\tilde{q}_L$). For the decay which gives the maximum value of $m_{q_{\rm f}ll}$, the LSP will have a non-zero momentum in the same direction as the sparticle sent out from the 'hardest' decay. There are three separate dominance regions in mass space where this happens, one for each sparticle decay in the cascade.

Consider the case where the second decay, that of $\tilde{\chi}_2^0$, is dominant. If $\tilde{\chi}_1^0$ cannot be brought to rest in the rest frame of $\tilde{q}_L$, the maximum value is obtained for the optimised case where $q_{\rm f}$ and $l_{\rm f}$ fly off in one direction and $l_{\rm n}$ in the opposite, see figure 8. In the last step of the figure all momenta are boosted back to the rest frame of $\tilde{q}_L$. If we are inside the dominance region, $\tilde{\chi}_1^0$ ends up with a momentum pointing 'upwards' in the rest frame of $\tilde{q}_L$, as in the figure. In this case the defining criterion of the region takes the form,

$$|\mathbf{p}_{l_{\rm n}}| > |\mathbf{p}_q + \mathbf{p}_{l_{\rm f}}| \quad \Rightarrow \quad \frac{m_{\tilde{\chi}_2^0}}{m_{\tilde{l}_R}} > \frac{m_{\tilde{l}_R}}{m_{\tilde{\chi}_1^0}} \frac{m_{\tilde{q}_L}}{m_{\tilde{\chi}_2^0}}\,, \tag{A.4}$$

where the three-momenta are taken in the rest frame of $\tilde{q}_L$. Note the form of the constraint in terms of *ratios of the masses of nearest neighbours in the decay chain.* The dominant ratio is the one which corresponds to the decay of $\tilde{\chi}_2^0$. The expression for $m_{q_{\rm f}ll}^{\rm max}$ in this region is then found by simply combining the four-momenta of the three Standard Model particles for the given *linear* configuration.

The defining inequality of the other two dominance regions and the resulting expressions for $m_{q_{\rm f}ll}^{\rm max}$ are found by similar approaches. The general result is again [12, eq. (4.4)]. Note the systematic pattern of inequalities which define the dominance regions. Although in cases *(1)* and *(3)* the right-hand side of the inequalities can be simplified, this was not done in order to emphasise the structure of the constraints.

The approach described above has some clear advantages over the more direct approach of method 1. Each region is 'understood' in terms of a dominant decay, here in the sense that the mass ratio is larger than the product of the other two, together with minimum momentum of $\tilde{\chi}_1^0$ in the rest frame of $\tilde{q}_L$. No angle α is needed. Only cascade decays on a line need be considered, which allows the entire calculation to be performed on a few sheets of paper.

Furthermore, and this is the most celebrated quality here, the approach is trivially extendable to an arbitrary number of particles. In particular, the solution for $m_{qqll}^{\max}$ is found in the same way, and is given in eq. (2.1). Notice the similarity with $m_{q_{\rm f}ll}^{\max}$. For a detailed calculation in the fully general case of a decay chain involving n sparticles, see [17].

B. Calculation of $m_{qql(\rm low)}^{\max}$

The calculation of $m_{qql(\rm low)}^{\max}$ turns out to be quite involved. This is a consequence of the inherent complexity of calculating 'low'-endpoints, joined with the many possible decay configurations available for the gluino decay chain. In order to demonstrate the peculiarities of 'low'-endpoints in a purer form, we first review the calculation of $m_{q_{\rm f}l(\rm low)}^{\max}$, the simplest of the 'low'-endpoints. For the calculation of $m_{qql(\rm low)}^{\max}$ which follow thereafter many of the considerations are similar, only significantly more difficult to carry through.

B.1 Preparations: review $m_{q_{\rm f}l(\rm low)}^{\max}$

Let us first recall that since there are two leptons, two invariant masses $m_{q_{\rm f}l}$ can be constructed, one of which will be higher than the other. These will be denoted the 'high' and 'low' distributions, each of which will have a maximum, denoted 'max'. Thus, the difficulty lies in identifying whether 'high' and 'low' correspond to the 'near' ($l_{\rm n}$) and 'far' ($l_{\rm f}$) leptons, or vice versa. The $m_{q_{\rm f}l(\rm high)}$ and $m_{q_{\rm f}l(\rm low)}$ distributions are constructed from the highest/lowest of $m_{q_{\rm f}l_{\rm n}}$ and $m_{q_{\rm f}l_{\rm f}}$ on an event by event basis. (We here assume that the correct jet has been selected.) Since the $m_{q_{\rm f}l}$ value which gives the absolute maximum must necessarily be the higher of $m_{q_{\rm f}l_{\rm n}}$ and $m_{q_{\rm f}l_{\rm f}}$ for the given configuration, we simply have $m_{q_{\rm f}l(\rm high)}^{\max} = \max(m_{q_{\rm f}l_{\rm n}}^{\max}, m_{q_{\rm f}l_{\rm f}}^{\max})$. For $m_{q_{\rm f}l(\rm low)}^{\max}$ the situation is more complicated; we need to look for the maximum value of the *lower* of $m_{q_{\rm f}l_{\rm n}}$ and $m_{q_{\rm f}l_{\rm f}}$. This conditional maximisation requires that both $m_{q_{\rm f}l}$ values are compared for the given configuration. Under no circumstance can the endpoint be higher than the lower of the two maxima, $m_{q_{\rm f}l(\rm low)}^{\max} \le \min(m_{q_{\rm f}l_{\rm n}}^{\max}, m_{q_{\rm f}l_{\rm f}}^{\max})$.

Let us first assume a mass scenario where $m_{q_{\rm f}l_{\rm n}}^{\max} < m_{q_{\rm f}l_{\rm f}}^{\max}$, which directly corresponds to the condition

$$m_{\tilde{l}_R}^2 > m_{\tilde{\chi}_1^0} m_{\tilde{\chi}_2^0}\,. \tag{B.1}$$

This is manifest in regions *(1)* and *(2)* of [12, eq. (4.5)]. Now, let us further assume that we have a decay configuration where $m_{q_{\rm f}l_{\rm n}}$ takes on its maximum value, $m_{q_{\rm f}l_{\rm n}} = m_{q_{\rm f}l_{\rm n}}^{\max}$, so that $q_{\rm f}$ and $l_{\rm n}$ are back-to-back in the rest frame of $\tilde{\chi}_2^0$. If it is possible to choose an orientation of $\mathbf{p}_{l_{\rm f}}$ such that $m_{q_{\rm f}l_{\rm f}} > m_{q_{\rm f}l_{\rm n}}$, then $m_{q_{\rm f}l_{\rm n}}$ can be a 'low'-value, and we will have $m_{q_{\rm f}l(\rm low)}^{\max} = m_{q_{\rm f}l_{\rm n}}^{\max}$. Specifically, this occurs when $m_{q_{\rm f}l_{\rm f}}$ takes on its maximum value, with $\mathbf{p}_{l_{\rm f}}$ in the opposite direction to $\mathbf{p}_{q_{\rm f}}$ (and parallel to $\mathbf{p}_{l_{\rm n}}$), which corresponds to

$$2m_{\tilde{l}_R}^2 > m_{\tilde{\chi}_1^0}^2 + m_{\tilde{\chi}_2^0}^2\,, \tag{B.2}$$

i.e. region *(1)* of [12, eq. (4.5)].

If this mass constraint is not satisfied, $m_{q_\mathrm{f}l_\mathrm{n}}$ will be the 'high'-value for any configuration which has $m_{q_\mathrm{f}l_\mathrm{n}} = m^{\max}_{q_\mathrm{f}l_\mathrm{n}}$ and $m_{q_\mathrm{f}l_\mathrm{f}}$ will be the 'low' value. To find the configuration which gives $m^{\max}_{q_\mathrm{f}l(\mathrm{low})}$ in this case, consider the more general situation where the angle α between $\mathbf{p}_{q_\mathrm{f}}$ and $\mathbf{p}_{l_\mathrm{n}}$ (in the rest frame of $\tilde{\chi}^0_2$) is reduced. The maximum value of $m_{q_\mathrm{f}l_\mathrm{f}}$ for this case is denoted $m^{\max}_{q_\mathrm{f}l_\mathrm{f}}(\alpha)$. (It will occur when $\mathbf{p}_{q_\mathrm{f}}$ and $\mathbf{p}_{l_\mathrm{f}}$ are back to back in the $\tilde{l}_R$ rest frame since $|\mathbf{p}_{l_\mathrm{f}}|$ obviously is independent of the orientation in this particular frame.) If α is reduced (starting from π), $m_{q_\mathrm{f}l_\mathrm{n}}(\alpha)$ will decrease and $m^{\max}_{q_\mathrm{f}l_\mathrm{f}}(\alpha)$ will increase. As α decreases, the 'high'-value decreases and the 'low'-value increases, and for some angle α_eq they become equal: $m_{q_\mathrm{f}l_\mathrm{n}}(\alpha_\mathrm{eq}) = m^{\max}_{q_\mathrm{f}l_\mathrm{f}}(\alpha_\mathrm{eq})$. If α is reduced below α_eq, $m_{q_\mathrm{n}l_\mathrm{n}}$ will become the 'low'-value, and as it decreases with α the 'low'-value will decrease. Hence, α_eq gives the optimal configuration, $m^{\max}_{q_\mathrm{f}l(\mathrm{low})} = m_{q_\mathrm{f}l_\mathrm{n}}(\alpha_\mathrm{eq}) \equiv m^{\max}_{q_\mathrm{f}l(\mathrm{eq})}$. A simple calculation gives eq. (4.8) of [12], and is valid for

$$m^2_{\tilde{\chi}^0_1} + m^2_{\tilde{\chi}^0_2} > 2m^2_{\tilde{l}_R}\,, \tag{B.3}$$

i.e. regions *(2)* and *(3)* of [12, eq. (4.5)].

One might expect to also find a separate solution for $m_{q_\mathrm{f}l_\mathrm{f}} < m_{q_\mathrm{f}l_\mathrm{n}}$ and $m_{q_\mathrm{f}l_\mathrm{f}} = m^{\max}_{q_\mathrm{f}l_\mathrm{f}}$, in analogy with the first solution obtained above. The situation is however not symmetric with respect to the two leptons. Maximisation of $m_{q_\mathrm{f}l_\mathrm{f}}$ necessarily fixes $m_{q_\mathrm{f}l_\mathrm{n}}$ at zero, so there is no third possibility, and once again $m^{\max}_{q_\mathrm{f}l(\mathrm{low})} = m^{\max}_{q_\mathrm{f}l(\mathrm{eq})}$. The general solution for $m^{\max}_{q_\mathrm{f}l(\mathrm{low})}$ is then given by two expressions, $m^{\max}_{q_\mathrm{f}l_\mathrm{n}}$ and $m^{\max}_{q_\mathrm{f}l(\mathrm{eq})}$, in the mass regions derived above, see [12, eq. (4.5)]. (Below, we will see that a third possibility is relevant for $m^{\max}_{qql(\mathrm{low})}$.)

B.2 $m^{\max}_{qql(\mathrm{low})}$: introduction

For a three-particle endpoint, the *configurations* which give the maximum values $m^{\max}_{qql_\mathrm{n}}$ and $m^{\max}_{qql_\mathrm{f}}$, as well as the endpoint expressions themselves, will be mass dependent (contrary to the situation for $m^{\max}_{q_\mathrm{f}l_\mathrm{n}}$ and $m^{\max}_{q_\mathrm{f}l_\mathrm{f}}$). In particular, we see from [12, eq. (4.4)] and eqs. (2.14) and (2.15) of this paper that there are four different cases (mass regions) for each. This increases the number of situations to consider, as well as the complexity for each.

To calculate $m^{\max}_{qql(\mathrm{low})}$ we use the same strategy as above. We will first investigate the situation $m_{qql_\mathrm{n}} < m_{qql_\mathrm{f}}$ with $m_{qql_\mathrm{n}} = m^{\max}_{qql_\mathrm{n}}$ (section B.3) and find the appropriate conditions on the masses corresponding to $m^{\max}_{qql(\mathrm{low})} = m^{\max}_{qql_\mathrm{n}}$. Then we will investigate the 'opposite' situation, $m_{qql_\mathrm{f}} < m_{qql_\mathrm{n}}$ with $m_{qql_\mathrm{f}} = m^{\max}_{qql_\mathrm{f}}$ (section B.4), and find the mass conditions for the solution $m^{\max}_{qql(\mathrm{low})} = m^{\max}_{qql_\mathrm{f}}$. This differs from $m^{\max}_{q_\mathrm{f}l(\mathrm{low})}$, where no such solution was available. Finally an 'equal'-solution will be sought (section B.5). It will consist of a critical-point solution and boundary solutions (at the boundary of a two-dimensional parameter space). The calculation of the 'equal'-solution is cumbersome and preferably performed with the aid of a computer program. The resulting expressions for the full solution are not very complicated, but many. Care should be taken in the implementation.

In the rest frame of $\tilde{\chi}^0_2$ the quark sector and the lepton sector can be described without reference to each other. This makes the $\tilde{\chi}^0_2$ rest frame particularly convenient to use. Unless stated otherwise, momenta and energies are given in this rest frame. The coordinate system

JHEP06(2005)015

$m_{qql_\mathrm{n}}^{\max}$	region condition	config. 1 $q_\mathrm{n} q_\mathrm{f}\ \ l_\mathrm{n} l_\mathrm{f}$	config. 2 $q_\mathrm{n} q_\mathrm{f}\ \ l_\mathrm{n} l_\mathrm{f}$
region *(1)*	$\frac{m_{\tilde g}}{m_{\tilde q_L}} > \frac{m_{\tilde q_L}}{m_{\tilde\chi_2^0}} \frac{m_{\tilde\chi_2^0}}{m_{\tilde l_R}}$	$\uparrow\downarrow\ \ \downarrow\uparrow$ superfluous	$\uparrow\downarrow\ \ \downarrow\downarrow$ trivial
region *(2)*	$\frac{m_{\tilde q_L}}{m_{\tilde\chi_2^0}} > \frac{m_{\tilde\chi_2^0}}{m_{\tilde l_R}} \frac{m_{\tilde g}}{m_{\tilde q_L}}$	$\downarrow\uparrow\ \ \downarrow\uparrow$ superfluous	$\downarrow\uparrow\ \ \downarrow\downarrow$ trivial
region *(3)*	$\frac{m_{\tilde\chi_2^0}}{m_{\tilde l_R}} > \frac{m_{\tilde g}}{m_{\tilde q_L}} \frac{m_{\tilde q_L}}{m_{\tilde\chi_2^0}}$	$\uparrow\uparrow\ \ \downarrow\uparrow$ no solution	$\uparrow\uparrow\ \ \downarrow\downarrow$ trivial
region *(4)*	otherwise	$\nwarrow\nearrow\ \ \downarrow\uparrow$ superfluous	$\nwarrow\nearrow\ \ \downarrow\downarrow$ trivial

Table 10: Possible configurations for $m_{qql_\mathrm{n}}^{\max}$. See the text for details.

will be chosen such that the combined momentum of the two quarks, $\mathbf{p}_{qq}$ will point upwards (along +z). The x and y components are not required, allowing the four-vectors to be given solely by the energy and the momentum in the z-direction.

B.3 $m_{qql(\mathrm{low})}^{\max} = m_{qql_\mathrm{n}}^{\max}$

We here investigate the situation $m_{qql_\mathrm{n}} < m_{qql_\mathrm{f}}$ with $m_{qql_\mathrm{n}} = m_{qql_\mathrm{n}}^{\max}$. The possible configurations with a maximised m_{qql_n} are given in table 10. The four rows correspond to the four different regions of mass-space appropriate to eq. (2.14) (i.e. [12, eq. (4.4)] with the substitution of eq. (2.14)), as labeled by the first column. The second column shows the corresponding 'region condition'. The third and fourth column show the directions of the quark and lepton momenta, from left to right as in the decay chain. The combined momentum of the quarks is always upwards (in the rest frame of $\tilde\chi_2^0$). The direction of $\mathbf{p}_{l_\mathrm{n}}$ is always downwards, while the direction of $\mathbf{p}_{l_\mathrm{f}}$ is upwards for configuration 1, downwards for configuration 2. Notice that in region *(4)*, configurations which correspond to a maximum of $m_{qql(\mathrm{low})}$ do *not* have the quarks aligned in the $\tilde\chi_2^0$ rest frame. There are four mass regions and two directions for $\mathbf{p}_{l_\mathrm{f}}$, giving in total eight possibilities. Each must be considered.

The comments 'trivial', 'no solution' and 'superfluous' give the conclusion of the investigations. Some of these are seen right away: in region *(3)*, configuration 1 the value of m_{qql_f} evidently vanishes since the three particles go in the same direction, hence m_{qql_f} must always be smaller than m_{qql_n} and there is 'no solution'. For configuration 2, in all four regions the condition $m_{qql_\mathrm{n}} < m_{qql_\mathrm{f}}$ is simply $|\mathbf{p}_{l_\mathrm{n}}| < |\mathbf{p}_{l_\mathrm{f}}|$, which 'trivially' corresponds to

$$m_{\tilde\chi_1^0}^2 + m_{\tilde\chi_2^0}^2 < 2m_{\tilde l_R}^2\,. \tag{B.4}$$

The three regions of configuration 1 which are marked 'superfluous' give mass conditions which turn out to be subsets of the corresponding ('trivial') mass condition of configuration 2 (when the appropriate region condition is also imposed). This means that if the ('superfluous') configuration 1 is possible, then also configuration 2 is possible. The conclusion of this subsection will therefore be that $m_{qll(\mathrm{low})}^{\max} = m_{qql_\mathrm{n}}^{\max}$ if and only if the trivial condition (B.4) is satisfied. The rest of the subsection is dedicated to proving that the superfluous conditions are indeed contained in the trivial one.

For each of the three regions we must first find the mass condition by requiring $m_{qql_\mathrm{n}} < m_{qql_\mathrm{f}}$. The proofs that these conditions are already contained in the trivial condition [given that the appropriate region conditions are also imposed], are carried through by combining these with the 'anti-trivial' condition, $m^2_{\tilde\chi^0_1}+m^2_{\tilde\chi^0_2} > 2m^2_{\tilde l_R}$, and see that this leads to contradictions. For regions *(1)* and *(2)* the proofs are fairly straightforward, but less so for region *(4)* due to the complicated nature of the region condition and the non-aligned quarks. Below we first find the mass conditions of the three regions, then show the proof for one of them. The proofs of the two others are similar.

Regions *(1)* and *(2)*. In the rest frame of $\tilde\chi^0_2$ the relevant four-vectors of configuration 1 are:

$$p_{qq} = (E_{qq},\ |\mathbf{p}_{qq}|)\,, \qquad p_{l_\mathrm{n}} = (|\mathbf{p}_{l_\mathrm{n}}|,\ -|\mathbf{p}_{l_\mathrm{n}}|)\,, \qquad p_{l_\mathrm{f}} = (|\mathbf{p}_{l_\mathrm{f}}|,\ |\mathbf{p}_{l_\mathrm{f}}|)\,, \tag{B.5}$$

where each entry is given in the form $(E,\ p_z)$. The condition we need to satisfy is then:

$$\begin{aligned} m_{qql_\mathrm{n}} < m_{qql_\mathrm{f}} &\Leftrightarrow (p_{qq}+p_{l_\mathrm{n}})^2 < (p_{qq}+p_{l_\mathrm{f}})^2 \Leftrightarrow p_{qq}\cdot p_{l_\mathrm{n}} < p_{qq}\cdot p_{l_\mathrm{f}} \\ &\Leftrightarrow (E_{qq}+|\mathbf{p}_{qq}|)|\mathbf{p}_{l_\mathrm{n}}| < (E_{qq}-|\mathbf{p}_{qq}|)|\mathbf{p}_{l_\mathrm{f}}|\,. \end{aligned} \tag{B.6}$$

The lepton three-momenta have the magnitude:

$$|\mathbf{p}_{l_\mathrm{n}}| = \frac{(m^2_{\tilde\chi^0_2} - m^2_{\tilde l_R})}{2m_{\tilde\chi^0_2}}\,, \qquad |\mathbf{p}_{l_\mathrm{f}}| = \frac{(m^2_{\tilde l_R} - m^2_{\tilde\chi^0_1})m_{\tilde\chi^0_2}}{2m^2_{\tilde l_R}} \tag{B.7}$$

For region *(1)* the quark sector gives

$$E_{qq} = |\mathbf{p}_{q_\mathrm{n}}| + |\mathbf{p}_{q_\mathrm{f}}|\,, \qquad |\mathbf{p}_{qq}| = |\mathbf{p}_{q_\mathrm{n}}| - |\mathbf{p}_{q_\mathrm{f}}| \tag{B.8}$$

$$E_{qq} + |\mathbf{p}_{qq}| = 2|\mathbf{p}_{q_\mathrm{n}}| = \frac{(m^2_{\tilde g} - m^2_{\tilde q_L})m_{\tilde\chi^0_2}}{m^2_{\tilde q_L}}\,, \qquad E_{qq} - |\mathbf{p}_{qq}| = 2|\mathbf{p}_{q_\mathrm{f}}| = \frac{(m^2_{\tilde q_L} - m^2_{\tilde\chi^0_2})}{m_{\tilde\chi^0_2}}\,. \tag{B.9}$$

For region *(2)*, the only difference is the expression for $|\mathbf{p}_{qq}|$, which differs by an overall sign ($|\mathbf{p}_{qq}| = |\mathbf{p}_{q_\mathrm{f}}| - |\mathbf{p}_{q_\mathrm{n}}|$), and amounts to interchanging the two expressions in (B.9). If the expressions for regions *(1)* and *(2)* are inserted into (B.6), the following mass conditions are found:

$$\text{region } (1): \quad m^2_{\tilde l_R}(m^2_{\tilde g} - m^2_{\tilde q_L})(m^2_{\tilde\chi^0_2} - m^2_{\tilde l_R}) < m^2_{\tilde q_L}(m^2_{\tilde q_L} - m^2_{\tilde\chi^0_2})(m^2_{\tilde l_R} - m^2_{\tilde\chi^0_1}) \tag{B.10}$$

$$\text{region } (2): \quad m^2_{\tilde q_L}m^2_{\tilde l_R}(m^2_{\tilde q_L} - m^2_{\tilde\chi^0_2})(m^2_{\tilde\chi^0_2} - m^2_{\tilde l_R}) < m^4_{\tilde\chi^0_2}(m^2_{\tilde g} - m^2_{\tilde q_L})(m^2_{\tilde l_R} - m^2_{\tilde\chi^0_1}) \tag{B.11}$$

If (B.10) or (B.11) is satisfied, together with the appropriate region condition (table 10, second column), then we have $m_{qql(\mathrm{low})}^{\max} = m_{qql_\mathrm{n}}^{\max}$.

Region *(4)***.** In region *(4)* the quarks are not sent out on a line (parallel/antiparallel). We must instead find p_{qq} in the rest frame of $\tilde{\chi}^0_2$ using the following equations:

$$(m_{\tilde{g}} - m_{\tilde{l}_R})^2 = p^2_{qql_{\rm n}} = p^2_{qq} + 2p_{qq} \cdot p_{l_{\rm n}} = E^2_{qq} - \mathbf{p}^2_{qq} + 2(E_{qq} + |\mathbf{p}_{qq}|)|\mathbf{p}_{l_{\rm n}}| \qquad \text{(B.12)}$$

$$m^2_{\tilde{g}} = p^2_{qq\tilde{\chi}^0_2} = p^2_{qq} + m^2_{\tilde{\chi}^0_2} + 2p_{\tilde{\chi}^0_2} \cdot p_{qq} = E^2_{qq} - \mathbf{p}^2_{qq} + m^2_{\tilde{\chi}^0_2} + 2m_{\tilde{\chi}^0_2} E_{qq} \,. \qquad \text{(B.13)}$$

The first equation uses the expression for $m^{\max}_{qql_{\rm n}}$ found in eq. (2.14). From these we find p_{qq}:

$$E_{qq} = \frac{m_{\tilde{g}}(m^2_{\tilde{\chi}^0_2} + m^2_{\tilde{l}_R}) - 2m^2_{\tilde{\chi}^0_2} m_{\tilde{l}_R}}{2m_{\tilde{\chi}^0_2} m_{\tilde{l}_R}} \,, \qquad |\mathbf{p}_{qq}| = \frac{m_{\tilde{g}}(m^2_{\tilde{\chi}^0_2} - m^2_{\tilde{l}_R})}{2m_{\tilde{\chi}^0_2} m_{\tilde{l}_R}} \qquad \text{(B.14)}$$

$$E_{qq} + |\mathbf{p}_{qq}| = \frac{m_{\tilde{\chi}^0_2}(m_{\tilde{g}} - m_{\tilde{l}_R})}{m_{\tilde{l}_R}} \,, \qquad E_{qq} - |\mathbf{p}_{qq}| = \frac{(m_{\tilde{g}} m_{\tilde{l}_R} - m^2_{\tilde{\chi}^0_2})}{m_{\tilde{\chi}^0_2}} \,. \qquad \text{(B.15)}$$

Insertion of these expressions into (B.6) gives the condition for region *(4)*:

$$m_{\tilde{l}_R}(m_{\tilde{g}} - m_{\tilde{l}_R})(m^2_{\tilde{\chi}^0_2} - m^2_{\tilde{l}_R}) < (m_{\tilde{g}} m_{\tilde{l}_R} - m^2_{\tilde{\chi}^0_2})(m^2_{\tilde{l}_R} - m^2_{\tilde{\chi}^0_1}) \,. \qquad \text{(B.16)}$$

If this is satisfied together with the corresponding region condition in the second column of table 10, then $m^{\max}_{qql({\rm low})} = m^{\max}_{qql_{\rm n}}$.

However, as stated earlier the mass conditions (B.10), (B.11) and (B.16) are 'superfluous'. Below this is proved for region *(1)*. From the region condition and the 'anti-trivial' condition, we have the following inequalities:

$$\frac{m_{\tilde{g}}}{m_{\tilde{q}_L}} > \frac{m_{\tilde{q}_L}}{m_{\tilde{\chi}^0_2}} \frac{m_{\tilde{\chi}^0_2}}{m_{\tilde{l}_R}} \Leftrightarrow m^2_{\tilde{l}_R}(m^2_{\tilde{g}} - m^2_{\tilde{q}_L}) > m^2_{\tilde{q}_L}(m^2_{\tilde{q}_L} - m^2_{\tilde{l}_R}) \qquad \text{(B.17)}$$

$$m^2_{\tilde{\chi}^0_1} + m^2_{\tilde{\chi}^0_2} > 2m^2_{\tilde{l}_R} \Leftrightarrow (m^2_{\tilde{\chi}^0_2} - m^2_{\tilde{l}_R}) > (m^2_{\tilde{l}_R} - m^2_{\tilde{\chi}^0_1}) \,. \qquad \text{(B.18)}$$

Starting from (B.10) and using (B.17)–(B.18) we can then write

$$\begin{aligned} m^2_{\tilde{q}_L}(m^2_{\tilde{q}_L} - m^2_{\tilde{\chi}^0_2})(m^2_{\tilde{l}_R} - m^2_{\tilde{\chi}^0_1}) \;&>\; m^2_{\tilde{l}_R}(m^2_{\tilde{g}} - m^2_{\tilde{q}_L})(m^2_{\tilde{\chi}^0_2} - m^2_{\tilde{l}_R}) \\ &>\; m^2_{\tilde{q}_L}(m^2_{\tilde{q}_L} - m^2_{\tilde{l}_R})(m^2_{\tilde{\chi}^0_2} - m^2_{\tilde{l}_R}) \\ &>\; m^2_{\tilde{q}_L}(m^2_{\tilde{q}_L} - m^2_{\tilde{l}_R})(m^2_{\tilde{l}_R} - m^2_{\tilde{\chi}^0_1}) \\ &\Rightarrow\; m_{\tilde{l}_R} > m_{\tilde{\chi}^0_2} \end{aligned} \qquad \text{(B.19)}$$

which is clearly wrong. Hence, given the correct region condition, the mass condition (B.10) is in contradiction to the anti-trivial condition, meaning that it must be contained in the trivial condition. Similar proofs apply for the two other superfluous cases.

We therefore have the following conclusion, as already stated: if (B.4) is satisfied, then $m^{\max}_{qll({\rm low})} = m^{\max}_{qql_{\rm n}}$.

B.4 $m^{\max}_{qql({\rm low})} = m^{\max}_{qql_{\rm f}}$

Here we investigate the situation $m_{qql_{\rm f}} < m_{qql_{\rm n}}$ with $m_{qql_{\rm f}} = m^{\max}_{qql_{\rm f}}$. The possible configurations with a maximised $m_{qql_{\rm f}}$ are given in table 11 (in contrast to table 10 where $m_{qql_{\rm n}}$ was maximised). As before we consider the rest frame of $\tilde{\chi}^0_2$ and align the coordinate

$m_{qql_\mathrm{f}}^{\max}$	region condition	config. 1 $q_\mathrm{n}q_\mathrm{f}\ \ l_\mathrm{n}l_\mathrm{f}$
region *(1)*	$\frac{m_{\tilde{g}}}{m_{\tilde{q}_L}} > \frac{m_{\tilde{q}_L}}{m_{\tilde{\chi}_2^0}} \frac{m_{\tilde{l}_R}}{m_{\tilde{\chi}_1^0}}$	$\uparrow\downarrow\ \ \uparrow\downarrow$ unique
region *(2)*	$\frac{m_{\tilde{q}_L}}{m_{\tilde{\chi}_2^0}} > \frac{m_{\tilde{l}_R}}{m_{\tilde{\chi}_1^0}} \frac{m_{\tilde{g}}}{m_{\tilde{q}_L}}$	$\downarrow\uparrow\ \ \uparrow\downarrow$ unique
region *(3)*	$\frac{m_{\tilde{l}_R}}{m_{\tilde{\chi}_1^0}} > \frac{m_{\tilde{g}}}{m_{\tilde{q}_L}} \frac{m_{\tilde{q}_L}}{m_{\tilde{\chi}_2^0}}$	$\uparrow\uparrow\ \ \uparrow\downarrow$ no solution
region *(4)*	otherwise	$\nwarrow\nearrow\ \ \uparrow\downarrow$ unique

Table 11: Possible configurations for $m_{qql_\mathrm{f}}^{\max}$. See the text for details.

system such as to have $\mathbf{p}_{qq}$ pointing upwards. The maximum value for m_{qql_f} is found for the decay configuration of $\tilde{\chi}_2^0$ and $\tilde{l}_R$ which maximises $\mathbf{p}_{l_\mathrm{f}}$ downwards (in the rest frame of $\tilde{\chi}_2^0$). This is achieved if first $\tilde{l}_R$, then l_f, are emitted downwards. Since this necessarily fixes $\mathbf{p}_{l_\mathrm{n}}$ upwards, there is only one configuration in table 11. The mass ratios in the quark sector are the same for $m_{qql_\mathrm{f}}^{\max}$ as for $m_{qql_\mathrm{n}}^{\max}$, but in the lepton sector the relevant ratio is now $m_{\tilde{\chi}_2^0}/(m_{\tilde{\chi}_1^0} m_{\tilde{\chi}_2^0}/m_{\tilde{l}_R}) = m_{\tilde{l}_R}/m_{\tilde{\chi}_1^0}$, see (2.14) and (2.15), which changes the region conditions in column 2 as compared to those of table 10.

Region *(3)* has no solution since m_{qql_n} vanishes and therefore cannot be the 'high'-value. In the three other regions there are unique mass conditions for the solution $m_{qql(\mathrm{low})}^{\max} = m_{qql_\mathrm{f}}^{\max}$, which is what we seek here. The calculations follow the exact same path as in the previous subsection.

Regions *(1)* **and** *(2)***.** In the rest frame of $\tilde{\chi}_2^0$ the relevant four-vectors are (compare with (B.5)):

$$p_{qq} = (E_{qq},\ |\mathbf{p}_{qq}|)\,, \qquad p_{l_\mathrm{n}} = (|\mathbf{p}_{l_\mathrm{n}}|,\ |\mathbf{p}_{l_\mathrm{n}}|)\,, \qquad p_{l_\mathrm{f}} = (|\mathbf{p}_{l_\mathrm{f}}|,\ -|\mathbf{p}_{l_\mathrm{f}}|)\,. \tag{B.20}$$

The condition we need to satisfy is now:

$$\begin{aligned} m_{qql_\mathrm{f}} < m_{qql_\mathrm{n}} &\Leftrightarrow (p_{qq}+p_{l_\mathrm{f}})^2 < (p_{qq}+p_{l_\mathrm{n}})^2 \Leftrightarrow p_{qq}\cdot p_{l_\mathrm{f}} < p_{qq}\cdot p_{l_\mathrm{n}} \\ &\Leftrightarrow (E_{qq}+|\mathbf{p}_{qq}|)|\mathbf{p}_{l_\mathrm{f}}| < (E_{qq}-|\mathbf{p}_{qq}|)|\mathbf{p}_{l_\mathrm{n}}|\,. \end{aligned} \tag{B.21}$$

The lepton momenta are still given by (B.7). The energy and momentum of the quarks are the same as in the previous subsection: eq. (B.9) for region *(1)*, the expressions interchanged for region *(2)*.

When these expressions are inserted into (B.21), we find the following mass conditions:

$$\text{region } (1){:}\quad m_{\tilde{\chi}_2^0}^4 (m_{\tilde{g}}^2 - m_{\tilde{q}_L}^2)(m_{\tilde{l}_R}^2 - m_{\tilde{\chi}_1^0}^2) < m_{\tilde{q}_L}^2 m_{\tilde{l}_R}^2 (m_{\tilde{q}_L}^2 - m_{\tilde{\chi}_2^0}^2)(m_{\tilde{\chi}_2^0}^2 - m_{\tilde{l}_R}^2) \tag{B.22}$$
$$\text{region } (2){:}\quad m_{\tilde{q}_L}^2 (m_{\tilde{q}_L}^2 - m_{\tilde{\chi}_2^0}^2)(m_{\tilde{l}_R}^2 - m_{\tilde{\chi}_1^0}^2) < m_{\tilde{l}_R}^2 (m_{\tilde{g}}^2 - m_{\tilde{q}_L}^2)(m_{\tilde{\chi}_2^0}^2 - m_{\tilde{l}_R}^2)\,. \tag{B.23}$$

If (B.22) or (B.23) is satisfied, together with the appropriate region condition (table 11, second column), then we have $m_{qql(\mathrm{low})}^{\max} = m_{qql_\mathrm{f}}^{\max}$.

JHEP06(2005)015

Region *(4)*. In region *(4)* the combination of

$$\left(m_{\tilde{g}}-\frac{m_{\tilde{\chi}_1^0}m_{\tilde{\chi}_2^0}}{m_{\tilde{l}_R}}\right)^2=p_{qql_{\rm f}}^2=p_{qq}^2+2p_{qq}\cdot p_{l_{\rm f}}=E_{qq}^2-\mathbf{p}_{qq}^2+2(E_{qq}+|\mathbf{p}_{qq}|)|\mathbf{p}_{l_{\rm f}}| \tag{B.24}$$

(equivalent to (B.12)) with (B.13) results in:

$$E_{qq}=\frac{m_{\tilde{g}}(m_{\tilde{l}_R}^2+m_{\tilde{\chi}_1^0}^2)-2m_{\tilde{\chi}_2^0}m_{\tilde{l}_R}m_{\tilde{\chi}_1^0}}{2m_{\tilde{l}_R}m_{\tilde{\chi}_1^0}}, \qquad |\mathbf{p}_{qq}|=\frac{m_{\tilde{g}}(m_{\tilde{l}_R}^2-m_{\tilde{\chi}_1^0}^2)}{2m_{\tilde{l}_R}m_{\tilde{\chi}_1^0}} \tag{B.25}$$

$$E_{qq}+|\mathbf{p}_{qq}|=\frac{(m_{\tilde{g}}m_{\tilde{l}_R}-m_{\tilde{\chi}_2^0}m_{\tilde{\chi}_1^0})}{m_{\tilde{\chi}_1^0}}, \qquad E_{qq}-|\mathbf{p}_{qq}|=\frac{(m_{\tilde{g}}m_{\tilde{\chi}_1^0}-m_{\tilde{\chi}_2^0}m_{\tilde{l}_R})}{m_{\tilde{l}_R}} \tag{B.26}$$

Insertion of these expressions into (B.21) gives the condition for region *(4)*:

$$m_{\tilde{\chi}_2^0}^2(m_{\tilde{g}}m_{\tilde{l}_R}-m_{\tilde{\chi}_2^0}m_{\tilde{\chi}_1^0})(m_{\tilde{l}_R}^2-m_{\tilde{\chi}_1^0}^2)<m_{\tilde{l}_R}m_{\tilde{\chi}_1^0}(m_{\tilde{g}}m_{\tilde{\chi}_1^0}-m_{\tilde{\chi}_2^0}m_{\tilde{l}_R})(m_{\tilde{\chi}_2^0}^2-m_{\tilde{l}_R}^2)\,. \tag{B.27}$$

If this is satisfied together with the corresponding region condition, then $m_{qql(\rm low)}^{\max}=m_{qql_{\rm f}}^{\max}$.

This result completes the special-case solutions of $m_{qql(\rm low)}^{\max}$.

B.5 $m_{qql(\rm low)}^{\max}=m_{qql(\rm eq)}^{\max}$

If none of the above mass conditions are fulfilled, the maximum of $m_{qql(\rm low)}$ will in general be reached in an 'equal-solution' decay configuration, where $m_{qql_{\rm n}}=m_{qql_{\rm f}}$.

The relevant information on the two first steps of the cascade decay is contained in the value of $|\mathbf{p}_{qq}|$. (We stay in the rest frame of $\tilde{\chi}_2^0$.) Its maximum value is attained if $q_{\rm n}$ and $q_{\rm f}$ are sent off in the same direction, and is given by

$$|\mathbf{p}_{qq}^{\uparrow\uparrow}|=\frac{m_{\tilde{g}}^2-m_{\tilde{\chi}_2^0}^2}{2m_{\tilde{\chi}_2^0}}\,. \tag{B.28}$$

If sent off in opposite directions, $|\mathbf{p}_{qq}|$ is at its minimum,

$$|\mathbf{p}_{qq}^{\uparrow\downarrow}|=\frac{|m_{\tilde{g}}^2m_{\tilde{\chi}_2^0}^2-m_{\tilde{q}_L}^4|}{2m_{\tilde{q}_L}^2m_{\tilde{\chi}_2^0}}\,. \tag{B.29}$$

In the following we let $|\mathbf{p}_{qq}|$ be a free variable and only later impose the physical constraint $|\mathbf{p}_{qq}|\in[|\mathbf{p}_{qq}^{\uparrow\downarrow}|,|\mathbf{p}_{qq}^{\uparrow\uparrow}|]$.

As before, we align the coordinate system to have $\mathbf{p}_{qq}$ along +z. The first lepton, $l_{\rm n}$, is emitted at an angle α relative to $\mathbf{p}_{qq}$. The direction of the second lepton, $l_{\rm f}$, is chosen to maximise $m_{qql_{\rm f}}$ for the given α, allowing the notation $m_{qql_{\rm f}}^{\max}(\alpha)$. We have this freedom since we are interested in the maximum, not just any $m_{qql(\rm eq)}$ value. At this stage the decay is parametrised in terms of two variables, $|\mathbf{p}_{qq}|$ and α. By requiring $m_{qql_{\rm n}}(\alpha)=m_{qql_{\rm f}}^{\max}(\alpha)$, the angle can be expressed in terms of $|\mathbf{p}_{qq}|$:

$$\cos\alpha_{\rm eq}=\frac{m_{\tilde{l}_R}^2\big(m_{\tilde{\chi}_1^0}^2+m_{\tilde{\chi}_2^0}^2-2m_{\tilde{l}_R}^2\big)\big(\sqrt{m_{\tilde{g}}^2+|\mathbf{p}_{qq}|^2}-m_{\tilde{\chi}_2^0}\big)-m_{\tilde{\chi}_2^0}\big(m_{\tilde{l}_R}^2-m_{\tilde{\chi}_1^0}^2\big)\varphi(|\mathbf{p}_{qq}|)}{\big(m_{\tilde{\chi}_2^0}^2-m_{\tilde{l}_R}^2\big)\big(2m_{\tilde{l}_R}^2-m_{\tilde{\chi}_1^0}^2\big)|\mathbf{p}_{qq}|}, \tag{B.30}$$

where $\varphi(|\mathbf{p}_{qq}|)$ is given by

$$\varphi(|\mathbf{p}_{qq}|)=\left[m^2_{\tilde\chi^0_2}|\mathbf{p}_{qq}|^2+\left(m^2_{\tilde\chi^0_1}+m^2_{\tilde\chi^0_2}-2m^2_{\tilde l_R}\right)\left(m^2_{\tilde g}+m^2_{\tilde\chi^0_2}-2m_{\tilde\chi^0_2}\sqrt{m^2_{\tilde g}+|\mathbf{p}_{qq}|^2}\right)\right]^{1/2} \quad \text{(B.31)}$$

(Later we will need to ensure that $|\cos\alpha_{\rm eq}|\le 1$.) Insertion of this solution into $m_{qql_{\rm n}}(\alpha)$ (or $m^{\max}_{qql_{\rm f}}(\alpha)$) returns an expression for $m_{qql(\rm eq)}$ in terms of $|\mathbf{p}_{qq}|$ only. Since we are interested in a maximum value we now search for the critical point of $m_{qql(\rm eq)}$, and find an expression for the critical momentum,

$$\begin{aligned}|\mathbf{p}^{\rm crit}_{qq}| =& \left[\left(2m_{\tilde l_R}(m^2_{\tilde\chi^0_1}+m^2_{\tilde\chi^0_2}-2m^2_{\tilde l_R})+(3m^2_{\tilde l_R}-m^2_{\tilde\chi^0_1})\sqrt{m^2_{\tilde g}+2m^2_{\tilde l_R}-m^2_{\tilde\chi^0_1}-m^2_{\tilde\chi^0_2}}\right)^2-\right.\\ &\left.-4m^2_{\tilde g}m^2_{\tilde\chi^0_2}m^2_{\tilde l_R}\right]^{1/2}\frac{1}{2m_{\tilde\chi^0_2}m_{\tilde l_R}} \end{aligned} \quad \text{(B.32)}$$

Inserting this back into $m_{qql(\rm eq)}$ gives an expression for the critical point solution,

$$\begin{aligned}\left(m^{\rm crit}_{qql(\rm eq)}\right)^2 =& m^2_{\tilde g}-\left[m_{\tilde\chi^0_2}(3m^2_{\tilde l_R}-m^2_{\tilde\chi^0_1})\sqrt{|\mathbf{p}^{\rm crit}_{qq}|^2+m^2_{\tilde g}}-\right.\\ &\left.-m^2_{\tilde\chi^0_2}m^2_{\tilde l_R}-(m^2_{\tilde l_R}-m^2_{\tilde\chi^0_1})\varphi(|\mathbf{p}^{\rm crit}_{qq}|)\right]/(2m^2_{\tilde l_R}-m^2_{\tilde\chi^0_1}). \end{aligned} \quad \text{(B.33)}$$

All expressions found from the procedure above are formal. In order for them to be physical, the momentum and the angle α of the critical solution must lie in the allowed regions:

$$|\mathbf{p}^{\rm crit}_{qq}| \in [|\mathbf{p}^{\uparrow\downarrow}_{qq}|, |\mathbf{p}^{\uparrow\uparrow}_{qq}|] \quad \text{(B.34)}$$

$$\cos\alpha_{\rm eq}(|\mathbf{p}^{\rm crit}_{qq}|) \in [-1,1] \quad \text{(B.35)}$$

For a given set of masses eqs. (B.34) and (B.35) must be tested numerically for the resulting $|\mathbf{p}^{\rm crit}_{qq}|$.

If the critical solution is *not* physical, the maximum must lie on the boundary of the two-dimensional domain defined by eqs. (B.34) and (B.35). For $\cos\alpha_{\rm eq}=\pm1$ the appropriate $|\mathbf{p}_{qq}|$ can be found by redoing the procedure leading to (B.33) but with α fixed at 0 or π. This gives the following expression for $|\mathbf{p}_{qq}|$:

$$\begin{aligned}|\mathbf{p}^{\cos\alpha=\pm1}_{qq}| =& \frac{\pm(m^2_{\tilde\chi^0_1}m^2_{\tilde\chi^0_2}-m^4_{\tilde l_R})}{4m_{\tilde\chi^0_2}m^2_{\tilde l_R}(m^2_{\tilde\chi^0_2}-m^2_{\tilde l_R})(m^2_{\tilde l_R}-m^2_{\tilde\chi^0_1})}\times\\ &\times\left[-(2m^2_{\tilde\chi^0_2}m^2_{\tilde l_R}-m^2_{\tilde\chi^0_1}m^2_{\tilde\chi^0_2}-m^4_{\tilde l_R})+\right.\\ &\left.+\sqrt{(m^2_{\tilde\chi^0_1}m^2_{\tilde\chi^0_2}-m^4_{\tilde l_R})^2+4m^2_{\tilde g}m^2_{\tilde l_R}(m^2_{\tilde\chi^0_2}-m^2_{\tilde l_R})(m^2_{\tilde l_R}-m^2_{\tilde\chi^0_1})}\right]. \end{aligned} \quad \text{(B.36)}$$

The invariant mass can then be found straightforward by taking $m^2_{qql_{\rm n}}=(p_{qq}+p_{l_{\rm n}})^2$ and using (B.13). This gives

$$\left(m^{\cos\alpha=\pm1}_{qql(\rm eq)}\right)^2 = \left[(m^2_{\tilde g}+m^2_{\tilde l_R})m_{\tilde\chi^0_2}-(m^2_{\tilde\chi^0_2}+m^2_{\tilde l_R})\sqrt{|\mathbf{p}^{\cos\alpha=\pm1}_{qq}|^2+m^2_{\tilde g}}\mp\right.$$

$$\mp (m^2_{\tilde\chi^0_2} - m^2_{\tilde l_R})|\mathbf{p}^{\cos\alpha=\pm1}_{qq}|\big]/m_{\tilde\chi^0_2}\,. \tag{B.37}$$

The boundary solutions at maximum and minimum $|\mathbf{p}_{qq}|$ are most easily found by inserting the boundary values (B.28)–(B.29) into the general solution (B.33). This gives

$$\left(m^{\uparrow\uparrow}_{qql(\mathrm{eq})}\right)^2 = (m^2_{\tilde g} - m^2_{\tilde\chi^0_2})\frac{(m^2_{\tilde l_R} - m^2_{\tilde\chi^0_1})}{(2m^2_{\tilde l_R} - m^2_{\tilde\chi^0_1})} \tag{B.38}$$

$$\begin{aligned}\left(m^{\uparrow\downarrow}_{qql(\mathrm{eq})}\right)^2 = \Big[&-(3m^2_{\tilde l_R} - m^2_{\tilde\chi^0_1})(m^2_{\tilde g}m^2_{\tilde\chi^0_2} + m^4_{\tilde q_L}) + 2m^2_{\tilde q_L}[m^2_{\tilde g}(2m^2_{\tilde l_R} - m^2_{\tilde\chi^0_1}) + m^2_{\tilde\chi^0_2}m^2_{\tilde l_R}] + \\ &+ 2m^2_{\tilde q_L}(m^2_{\tilde l_R} - m^2_{\tilde\chi^0_1})\varphi(|\mathbf{p}^{\uparrow\downarrow}_{qq}|)\Big]/[2m^2_{\tilde q_L}(2m^2_{\tilde l_R} - m^2_{\tilde\chi^0_1})]\,.\end{aligned} \tag{B.39}$$

All expressions (B.37)–(B.39) are formal. For a given set of masses one must explicitly (numerically) impose the one of eqs. (B.34) and (B.35) which is not satisfied by construction.

B.6 General solution

Putting all this together, the fully general solution for $m^{\max}_{qql(\mathrm{low})}$ is given by

$$m^{\max}_{qql(\mathrm{low})} = \begin{cases} m^{\max}_{qql_{\mathrm{n}}} & \text{for} \quad m^2_{\tilde\chi^0_1} + m^2_{\tilde\chi^0_2} < 2m^2_{\tilde l_R} \\ m^{\max}_{qql_{\mathrm{f}}} & \text{for} \quad \langle\mathrm{cut1}\rangle \\ m^{\max}_{qql(\mathrm{eq})} & \text{otherwise,} \end{cases} \tag{B.40}$$

where

$$\begin{aligned}\langle\mathrm{cut1}\rangle = \; &\left[\frac{m_{\tilde g}}{m_{\tilde q_L}} > \frac{m_{\tilde q_L}}{m_{\tilde\chi^0_2}}\frac{m_{\tilde l_R}}{m_{\tilde\chi^0_1}} \wedge \frac{m^4_{\tilde\chi^0_2}\left(m^2_{\tilde g} - m^2_{\tilde q_L}\right)\left(m^2_{\tilde l_R} - m^2_{\tilde\chi^0_1}\right)}{m^2_{\tilde q_L}m^2_{\tilde l_R}\left(m^2_{\tilde q_L} - m^2_{\tilde\chi^0_2}\right)\left(m^2_{\tilde\chi^0_2} - m^2_{\tilde l_R}\right)} < 1\right] \vee \\ \vee &\left[\frac{m_{\tilde q_L}}{m_{\tilde\chi^0_2}} > \frac{m_{\tilde l_R}}{m_{\tilde\chi^0_1}}\frac{m_{\tilde g}}{m_{\tilde q_L}} \wedge \frac{m^2_{\tilde q_L}\left(m^2_{\tilde q_L} - m^2_{\tilde\chi^0_2}\right)\left(m^2_{\tilde l_R} - m^2_{\tilde\chi^0_1}\right)}{m^2_{\tilde l_R}\left(m^2_{\tilde g} - m^2_{\tilde q_L}\right)\left(m^2_{\tilde\chi^0_2} - m^2_{\tilde l_R}\right)} < 1\right] \vee \\ \vee &\left[\frac{m_{\tilde g}}{m_{\tilde q_L}} < \frac{m_{\tilde q_L}}{m_{\tilde\chi^0_2}}\frac{m_{\tilde l_R}}{m_{\tilde\chi^0_1}} \wedge \frac{m_{\tilde q_L}}{m_{\tilde\chi^0_2}} < \frac{m_{\tilde l_R}}{m_{\tilde\chi^0_1}}\frac{m_{\tilde g}}{m_{\tilde q_L}} \wedge \frac{m_{\tilde l_R}}{m_{\tilde\chi^0_1}} < \frac{m_{\tilde g}}{m_{\tilde q_L}}\frac{m_{\tilde q_L}}{m_{\tilde\chi^0_2}}\right. \\ &\left.\wedge \frac{m^2_{\tilde\chi^0_2}\left(m_{\tilde g}m_{\tilde l_R} - m_{\tilde\chi^0_2}m_{\tilde\chi^0_1}\right)\left(m^2_{\tilde l_R} - m^2_{\tilde\chi^0_1}\right)}{m_{\tilde l_R}m_{\tilde\chi^0_1}\left(m_{\tilde g}m_{\tilde\chi^0_1} - m_{\tilde\chi^0_2}m_{\tilde l_R}\right)\left(m^2_{\tilde\chi^0_2} - m^2_{\tilde l_R}\right)} < 1\right]\end{aligned} \tag{B.41}$$

is constructed from (B.22), (B.23) and (B.27) together with the appropriate region conditions. Expressions for $m^{\max}_{qql_{\mathrm{n}}}$ and $m^{\max}_{qql_{\mathrm{f}}}$ are given in eqs. (2.14) and (2.15) respectively, and $m^{\max}_{qql(\mathrm{eq})}$ is given by

$$m^{\max}_{qql(\mathrm{eq})} = \max\left(m^{\mathrm{crit}}_{qql(\mathrm{eq})}, m^{\cos\alpha=\pm1}_{qql(\mathrm{eq})}, m^{\uparrow\uparrow}_{qql(\mathrm{eq})}, m^{\uparrow\downarrow}_{qql(\mathrm{eq})}\right) \tag{B.42}$$

which uses (B.33) and (B.37)–(B.39).

Acknowledgments

This work has been performed partly within the ATLAS Collaboration, and we thank collaboration members for helpful discussions. We have made use of the physics analysis framework and tools which are the results of collaboration-wide efforts. We are in particular grateful to Giacomo Polesello for numerous discussions. BKG would like to thank Steinar Stapnes for useful discussions. This research has been supported in part by the Research Council of Norway.

References

[1] P. Fayet and S. Ferrara, *Supersymmetry*, *Phys. Rept.* **32** (1977) 249.

[2] S. Dimopoulos and H. Georgi, *Softly broken supersymmetry and* SU(5), *Nucl. Phys.* **B 193** (1981) 150.

[3] H.P. Nilles, *Supersymmetry, supergravity and particle physics*, *Phys. Rept.* **110** (1984) 1.

[4] H.E. Haber and G.L. Kane, *The search for supersymmetry: probing physics beyond the standard model*, *Phys. Rept.* **117** (1985) 75.

[5] S. Weinberg, *Implications of dynamical symmetry breaking*, *Phys. Rev.* **D 13** (1976) 974; *Implications of dynamical symmetry breaking: an addendum*, *Phys. Rev.* **D 19** (1979) 1277; L. Susskind, *Dynamics of spontaneous symmetry breaking in the Weinberg- Salam theory*, *Phys. Rev.* **D 20** (1979) 2619;
G. 't Hooft, in *Recent developments in gauge theories*, Proceedings of the NATO Advanced Summer Institute, Cargese 1979, G. 't Hooft *et al.* ed., Plenum, New York 1980

[6] I. Hinchliffe, F.E. Paige, M.D. Shapiro, J. Soderqvist and W. Yao, *Precision SUSY measurements at LHC*, *Phys. Rev.* **D 55** (1997) 5520 [hep-ph/9610544].

[7] I. Hinchliffe, F. E. Paige, E. Nagy, M. D. Shapiro, J. Soderqvist and W. Yao, *Precision SUSY measurements at LHC: Point 3*, LBNL-40954.

[8] H. Bachacou, I. Hinchliffe and F.E. Paige, *Measurements of masses in SUGRA models at LHC*, *Phys. Rev.* **D 62** (2000) 015009 [hep-ph/9907518].

[9] G. Polesello, *Precision SUSY measurements with ATLAS for SUGRA point 5*, ATLAS Internal Note, PHYS-No-111, October 1997.

[10] B.C. Allanach, C.G. Lester, M.A. Parker and B.R. Webber, *Measuring sparticle masses in non-universal string inspired models at the LHC*, *JHEP* **09** (2000) 004 [hep-ph/0007009].

[11] C.G. Lester, *Model independent sparticle mass measurements at ATLAS*, Ph. D. thesis, http://www.slac.stanford.edu/spires/find/hep/www?r=cern-thesis-2004-003.

[12] B.K. Gjelsten, D.J. Miller and P. Osland, *Measurement of SUSY masses via cascade decays for SPS 1a*, *JHEP* **12** (2004) 003 [hep-ph/0410303].

[13] B.C. Allanach *et al.*, *The snowmass points and slopes: benchmarks for SUSY searches*, *Eur. Phys. J.* **C 25** (2002) 113 [hep-ph/0202233].

JHEP06(2005)015

[14] B.K. Gjelsten, E. Lytken, D.J. Miller, P. Osland, G. Polesello, *A detailed analysis of the measurement of SUSY masses with the ATLAS detector at the LHC*, ATL-PHYS-2004-007, Geneva, CERN, Jan 2004;
LHC/LC Study Group collaboration, G. Weiglein *et al.*, *Physics interplay of the LHC and the ILC*, hep-ph/0410364.

[15] M.M. Nojiri, G. Polesello and D.R. Tovey, *Proposal for a new reconstruction technique for SUSY processes at the LHC*, hep-ph/0312317.

[16] P. Richardson, *Spin correlations in Monte Carlo simulations*, *JHEP* **11** (2001) 029 [hep-ph/0110108];
A.J. Barr, *Determining the spin of supersymmetric particles at the LHC using lepton charge asymmetry*, *Phys. Lett.* **B 596** (2004) 205 [hep-ph/0405052].

[17] B.K. Gjelsten, Ph. D. thesis, University of Oslo, 2005.

[18] H. Baer, F.E. Paige, S.D. Protopopescu and X. Tata, *Simulating supersymmetry with ISAJET 7.0/ISASUSY 1.0*, hep-ph/9305342;
H. Baer, F.E. Paige, S.D. Protopopescu and X. Tata, *Isajet 7.48: a Monte Carlo event generator for p p, $\bar{p}p$ and e^+e^- reactions*, hep-ph/0001086.

[19] T. Sjöstrand *et al.*, *High-energy-physics event generation with PYTHIA 6.1*, *Comput. Phys. Commun.* **135** (2001) 238 [hep-ph/0010017];
T. Sjöstrand, L. Lönnblad and S. Mrenna, *PYTHIA 6.2: physics and manual*, hep-ph/0108264.

[20] CTEQ collaboration, H.L. Lai *et al.*, *Global QCD analysis of parton structure of the nucleon: CTEQ5 parton distributions*, *Eur. Phys. J.* **C 12** (2000) 375 [hep-ph/9903282].

[21] E. Richter-Was, D. Froidevaux and L. Poggioli, *ATLFAST 2.0: a fast simulation package for ATLAS*, Tech. Rep. ATL-PHYS-98-131, 1998.

[22] F. James and M. Roos, *'MINUIT' a system for function minimization and analysis of the parameter errors and correlations*, *Comput. Phys. Commun.* **10** (1975) 343.

[23] ATLAS Collaboration, *ATLAS detector and physics performance technical design report*, vol. I, CERN-LHCC-99-014, May, 1999.

[24] ECFA/DESY LC Physics Working Group collaboration, J.A. Aguilar-Saavedra *et al.*, *TESLA technical design report part III. Physics at an e^+e^- linear collider*, hep-ph/0106315.

[25] B.C. Allanach *et al.*, *Reconstructing supersymmetric theories by coherent LHC/LC analyses*, hep-ph/0403133.

JHEP06(2005)015